Water Mass Transformation Budgets in Finite-Volume Generalized Vertical Coordinate Ocean Models

Henri. F. Drake[1], Shanice Bailey[2], Raphael Dussin[3,5], Stephen M. Griffies[4,5], John Krasting[5], Graeme MacGilchrist[6], Geoffrey Stanley[7], Jan-Erik Tesdal[4], Jan D. Zika[8,9]

[1]Department of Earth System Science, University of California Irvine, Irvine, CA, USA
[2]Columbia University, Department of Earth and Environmental Sciences, NY, USA
[3]University Corporation for Atmospheric Research, Boulder, CO, USA
[4]Princeton University Program in Atmospheric and Oceanic Sciences, Princeton, NJ, USA
[5]NOAA Geophysical Fluid Dynamics Laboratory, Princeton, NJ, USA
[6]School of Earth and Environmental Sciences, University of St. Andrews, Scotland
[7]School of Earth and Ocean Sciences, University of Victoria, Canada
[8]School of Mathematics and Statistics, University of New South Wales, Australia
[9]Australian Centre for Excellence in Antarctic Science, University of New South Wales, Australia

Key Points:

- Water mass budgets provide insights into the processes transforming material water mass properties and how they relate to circulation.
- Spurious water mass transformations due to advection scheme errors can be quantified by combining mass and tracer budget diagnostics.
- We describe best practices for model analysis and present a novel Python stack for model-agnostic and out-of-memory regional calculations.

Corresponding author: Henri Drake, `hfdrake@uci.edu`

Abstract

Water mass transformation theory provides conceptual tools that in principle enable innovative analyses of numerical ocean models; in practice, however, these methods can be challenging to implement and interpret, and therefore remain under-utilized. Our aim is to demonstrate the feasibility of diagnosing all terms in the water mass budget and to exemplify their usefulness for scientific inquiry and model development by quantitatively relating water mass changes, overturning circulations, boundary fluxes, and interior mixing.

We begin with a pedagogical derivation of key results of classical water mass transformation theory. We then describe best practices for diagnosing each of the water mass budget terms from the output of Finite-Volume Generalized Vertical Coordinate (FV-GVC) ocean models, including the identification of a non-negligible remainder term as the spurious numerical mixing due to advection scheme discretization errors. We illustrate key aspects of the methodology through an example application to diagnostics from a polygonal region of a Baltic Sea regional configuration of the Modular Ocean Model v6 (MOM6). We verify the convergence of our WMT diagnostics by brute-force, comparing time-averaged diagnostics on various vertical grids to timestep-averaged diagnostics on the native model grid. Finally, we briefly describe a stack of xarray-enabled Python packages for evaluating WMT budgets in FV-GVC models, which is intended to be model-agnostic and available for community use and development.

Plain Language Summary

A useful tool for characterizing ocean variability and change is water mass analysis, in which the ocean is decomposed into parcels with distinct properties (such as their temperature, density, or dissolved oxygen concentrations). Water mass transformation theory provides a concise equation for the evolution of these water masses, which can be used to identify the various processes that act to increase or decrease the total mass (or size) of each parcel. In practice, however, calculating the terms in these WMT budget equations from ocean model simulation output is technically challenging, limiting the creativity of applications in the literature. We review the fundamentals of water mass transformation theory, explain how to calculate WMT budgets based on the output of a generic ocean model simulation (with examples from a widely used one), and summarize a new publicly-available software for doing such calculations.

1 Introduction

The mean state, intrinsic variability, and forced changes of the global ocean can be usefully characterized by dividing waters into several distinct *water masses* and analyzing their respective steady balances or transient evolutions (Sverdrup et al., 1942). Each such water mass is defined by the intersection of bounds on scalar tracer concentrations and/or fixed spatial coordinates that define a region of the globe. (For convenience, we use the term 'water mass' to refer to both the region that it occupies in space, Ω, as well as the total mass of seawater in the region, $\mathcal{M}_\Omega$; it will be clear which is meant from context and notation.) The ocean's global overturning circulation, for example, is canonically described as the circulation of water masses through latitude-density space (Döös & Webb, 1994; Lumpkin & Speer, 2007; Cessi, 2019). Since density variations exert a significant control on oceanic flow, it is common to categorizing water masses in distinct density classes. Seawater density itself depends nonlinearly on temperature and salinity (and pressure), which due to their different boundary conditions are partially independent and are thus used to further distinguish water masses. Passive tracers, especially dissolved or particulate biogeochemical substances, also serve as effective water mass tags (Broecker, 1982). We focus here on water masses defined by bounds on a single scalar (e.g., temperature, density, or tracer concentration) but acknowledge that it can be beneficial to consider the intersections of bounds on multiple tracers (e.g., to analyze the thermohaline streamfunction as in Zika et al. (2012); Döös et al. (2012); Groeskamp et al. (2014)). Throughout the text, we denote surfaces of constant scalar values as *iso*scalar surfaces and the direction normal to isoscalar surfaces (in the direction of increasing scalar value) as *dia*scalar.

In water mass analysis, ocean variability and change is understood as the variability and change of its constituent water *masses*. Kinematically, water mass change refers to the movement of the isoscalar surfaces that bound the water mass. For instance, the observed contraction of Antarctic Bottom Waters corresponds to the deepening of their bounding isopycnal surface due to decades of abyssal warming and freshening (Purkey & Johnson, 2012). The utility of a particular tracer for water mass analysis depends on how its source/sink and transport processes relate to the problem at hand. Water mass analysis has long been used by oceanographers to infer patterns of large-scale ocean circulation from tracers with long residence times and known sources/sinks. Early analyses (e.g., Iselin (1939)) were carried out qualitatively and by hand, while more recent analyses employ numerical models on fixed Eulerian grids.

A major conceptual breakthrough was Walin (1982)'s introduction of Water Mass Transformation (WMT) theory, which directly equates the kinematic evolution and circulation of water masses to the various transformation processes that drive material change. Tziperman (1986), A. J. G. Nurser et al. (1999), Marshall et al. (1999), Iudicone et al. (2008) and others further developed important aspects of the theory. Groeskamp et al. (2019) present a modern treatment of WMT fundamentals and review various applications in the literature; our purpose here is not to repeat this exercise but instead to complement it by detailing how each of the terms in a water mass budget should be diagnosed and interpreted in the context of finite-volume ocean models. Calculations of full water mass transformation budgets are rare in the literature, reflecting the scarcity of necessary diagnostics and the technical difficulty of implementing methods consistent with increasingly complicated numerical model formulations. The difficulty of closing WMT budgets motivates a common use case, which is to assume a closed budget and simply bundle any neglected terms into a remainder (e.g. Tesdal et al., 2023; Evans et al., 2023). Many go even further, assuming the water mass distribution to be in steady state and thus identifying the remainder of the water mass transformation terms as the diascalar overturning transport (de Lavergne et al., 2016; Ferrari et al., 2016). A major caveat of all these indirect inference approaches is that any errors in the explicitly calculated terms–whether observational, computational, or conceptual in nature–are obscured by bundling them into the remainder along with the neglected terms; this total remainder term is often found to be of leading order, calling into question interpretations of WMT budget results. A more careful analysis would evaluate every term in the budget and confirm that the remainder is zero–or at least sufficiently small to not affect the interpretation of results (see Lele et al. (2021) for an observation-based example of an approximately closed full WMT budget).

A related but more subtle problem with model-based water mass analysis regards spurious water mass transformation due to numerical mixing, which is the effective diascalar mixing induced by artificial diffusive and dispersive errors in a discretized tracer advection scheme (Molenkamp, 1968). Spurious water mass transformations in density space (i.e. diapycnal) are particularly concerning because diapycnal mixing plays a leading-order role in ocean dynamics and energetics (Toggweiler & Samuels, 1998; Ferrari & Wunsch, 2009) and because measured diapycnal mixing rates are small enough that they can be easily overwhelmed by numerical errors (Griffies et al., 2000; Lee et al., 2002). Current-generation ocean and climate models still suffer from significant biases which can be traced to excessive diapycnal mixing, much of which is thought to be due to spurious numerical mixing as opposed to over-tuned mixing parameterizations (Fox-Kemper et al., 2019). Reducing spurious diapycnal mixing thus remains a priority of ocean model development and a driver of major model configuration choices, such as the adoption of isopycnal or hybrid generalized vertical coordinates (e.g., Adcroft et al., 2019; Griffies et al., 2020). Despite the importance of numerical mixing for both the development of ocean models and their application for scientific research, there is no consensus on the best practices for quantifying it, and no open-source community diagnostics are presently available. Let us briefly review some of the key approaches for quantifying numerical mixing in the literature and describe each of their limitations, motivating our novel approach here.

In their formative analysis, Griffies et al. (2000) apply Winters et al. (1995)'s available potential energy-based framework to diagnose spurious diapycnal mixing from erroneous increases in background potential energy in explicitly 'adiabatic' idealized flows. This background potential energy approach is invasive in that it requires temporarily 'spinning down' a diabatic model in a counterfactual adiabatic configuration; a limitation of this approach is that the spurious mixing inferred from the adiabatic configuration does not necessarily correspond to that of the diabatic configuration of interest. Ilıcak et al. (2012) apply this method to a suite of idealized and realistic ocean model configurations, and demonstrate that numerical mixing is highest in an eddying depth-coordinate model. The interpretation of such results requires additional humility, however, because the calculation of background potential energy by globally sorting the density field is ill-posed for global ocean models with nonlinear equations of state and topography that dynamically decouples ocean basins (Huang, 2005; Stewart et al., 2014; Saenz et al., 2015).Hill et al. (2012) propose an approach based on the diapycnal spreading of passive tracers; however, this approach is not scalable to global climate models configurations due to the many additional passive tracers that would need to be integrated. Drake et al. (2022) raise a more fundamental problem with the tracer-based approach: a tracer's diapycnal spreading rate is not exactly proportional to tracer-weighted diffusivity. Burchard and Rennau (2008) propose a tracer variance approach motivated by turbulence studies, which offers the means to map where spurious mixing occurs. However, it provides a three-dimensional effective diffusivity and so does not distinguish between diapycnal and isopycnal. Given these caveats and limitations of the above methods, we would like a more robust metric of spurious diascalar mixing that can be: 1) directly compared to parameterized diascalar mixing processes, 2) efficiently and unintrusively diagnosed, and 3) unambiguously interpreted.

Lee et al. (2002) pioneered a promising approach for diagnosing spurious diapycnal mixing as the remainder of a model's WMT budget, which in principle allows spurious mixing to be directly compared against other terms in the mass budget. Lee et al. (2002)'s analysis suggests that spurious diapycnal mixing is an order of magnitude larger than the parameterized vertical mixing in their model, although they invoke some questionable assumptions to close the mass budget without directly diagnosing transformations due to parameterized diffusion or surface fluxes. Megann (2018) improve upon this approach by directly comparing effective diapycnal transports with those implied by parameterized mixing, attributing the difference between the two to spurious numerical mixing. Urakawa and Hasumi (2012) and Urakawa and Hasumi (2014) extend the approach by evaluating every term in the WMT budget and identifying the remainder as the spurious water mass transformation, without resorting to approximations or expressing the results in terms of an 'effective' numerical diffusivity. (They additionally propose a method for decomposing spurious numerical mixing into cabbeling and non-cabbeling components, but this requires implementing intrusive new diagnostics, so we neglect it here for simplicity). Bailey et al. (2023) generalizes the approach from latitudinal coordinates to a rectangular region with vertical walls. An important caveat of the above WMT budget calculations is that they consider transformations across potential density surfaces (often referenced to either surface pressures $p = p_{\mathrm{atm}} \approx 0\,\mathrm{dbar}$, denoted ρ_0, or a mid-depth pressure of $2000\,\mathrm{dbar}$, denoted ρ_2). Because potential density surfaces deviate significantly from neutrality away from their reference pressure, purely isoneutral processes can misleadingly appear to induce diapycnal transformations, potentially leading to misinterpretation of results (see T. J. McDougall et al. (2014) as well as the discussion in Section 4). Iudicone et al. (2008) address these limitations by diagnosing water mass transformations across approximately neutral density γ^n surfaces (as defined by Jackett and McDougall (1997)); however, they do not diagnose all of the terms in the WMT budget and thus do not isolate the contributions from spurious numerical mixing. A practical limitation of each of these approaches is that the calculation of lateral transport terms is tailored to the particular analysis, such that it would take a considerable effort to replicate the analysis for 1) a different region, 2) a model with a different grid or budget diagnostics, or 3) with respect to a different tracer. Holmes et al. (2021) cleverly sidestep the two challenging aspects of WMT analysis described above–nonlinear equation of state effects and the diagnosis of lateral transports across complicated regional boundaries–by framing their analysis in terms of dia*thermal* fluxes and by diagnosing budget terms in *individual grid columns*.

We present a theoretically precise and numerically accurate approach for diagnosing closed WMT budgets in Finite-Volume ocean models with Generalized Vertical Coordinates (FV-GVC models). The following self-contained derivations of the theory are inspired by the water mass transformation framework introduced by Walin (1982), recently reviewed by Groeskamp et al. (2019), and extended to the numerical modeling context by Lee et al. (2002), Urakawa and Hasumi (2012), and Bailey et al. (2023). Because the derivations in these prior texts leave out many details and pass over some important theoretical and practical aspects of water mass analysis, we present a more complete and pedagogical derivation of the fundamental equations of water mass analysis. We argue that this level of care is necessary to 1) correctly close regional WMT budgets, 2) confidently attribute the remainder term to spurious numerical mixing, and 3) robustly interpret the balance of terms in the budget.

Section 2 presents the continuous theory and Section 3 describes how each of these terms is diagnosed in practice, including the identification of the remainder term with spurious numerical mixing (Section 3.5). Section 4 concludes with a future outlook discussion, including discussions of unconventional WMT analyses and important subtleties of WMT calculations in density space. Appendix A describes the relationship between the continuous theory (Section 2) and the layer-integrated mass and tracer budget diagnostics provided by FV-GVC models (used for the calculations in Section 3). Appendix B describes how these terms correspond to diagnostics available in the Modular Ocean Model v6 (MOM6; Adcroft et al. (2019)). In Appendix C we discuss some theoretical aspects of WMT budgets under the Boussinesq approximation, which is employed by many commonly used FV-GVC ocean models and often assumed in WMT analyses. Appendix D describes the core open-source Python package (`xwmb`) developed to carry out these WMT budget calculations, as well as the stack of packages it depends on, which are all intended to be model-agnostic and available for use by the ocean modeling community. Throughout, we provide illustrations of theoretical concepts and examples of numerical calculations based on diagnostics from a year-long ocean-only simulation in a regional Baltic Sea configuration of MOM6 at a nominal horizontal grid spacing of 0.25°. Ongoing extensions of the work to global OM4 (Adcroft et al., 2019) and CM4 (Held et al., 2019) outputs and approximately neutral density coordinates (following Stanley et al. (2021)) are beyond the scope of this paper and will be described elsewhere.

2 Theory: kinematics of λ-water masses and their transformations

2.1 Evolution of λ-water masses

We are interested in the evolution of bulk water masses defined by contours $\{\tilde{\lambda}\}$ of a single given scalar $\lambda(\mathbf{x}, t)$, which we here define as the class of waters with $\lambda(\boldsymbol{x}, t) \leq$

$\tilde{\lambda}$. The key metric that characterizes a water mass is, unsurprisingly, its mass

$$\mathcal{M}(\tilde{\lambda}, t) \equiv \int\limits_{\lambda(\boldsymbol{x},t) \leq \tilde{\lambda}} \rho \, \mathrm{d}V, \tag{1}$$

where $\rho(\boldsymbol{x}, t)$ is the seawater density *in situ* and $\mathrm{d}V$ is the volume element. More generally, we can consider the intersection $\Omega(\tilde{\lambda}, t) \equiv \{\boldsymbol{x} : \lambda(\boldsymbol{x}, t) < \tilde{\lambda}\} \cap \mathcal{R}$ of this global water mass definition with an arbitrary time-varying spatial region of the ocean, $\mathcal{R}(t)$. We emphasize that the water mass region Ω need not be contiguous. The water mass region Ω is characterized by the sub-mass

$$\mathcal{M}_{\Omega}(\tilde{\lambda}, t) \equiv \int\limits_{\Omega(\tilde{\lambda},t)} \rho \, \mathrm{d}V \leq \mathcal{M}(\tilde{\lambda}, t). \tag{2}$$

For example, if $\mathcal{R}$ is the Southern Ocean south of 30°S, then we identify $\Omega(1\,°\mathrm{C}, t) = \{\boldsymbol{x} : \Theta(\boldsymbol{x}, t) < 1\,°\mathrm{C}\} \cap \mathcal{R}$ as the mass of cold waters around Antarctica.

The complementary water mass that is instead bounded from below, $\mathcal{M}^{\dagger}_{\Omega}(\tilde{\lambda}, t) \equiv \int_{\tilde{\lambda}<\lambda} \rho \, \mathrm{d}V$, is simply derived as $\mathcal{M}^{\dagger}_{\Omega}(\tilde{\lambda}, t) = \mathcal{M}_{\mathcal{R}} - \mathcal{M}_{\Omega}(\tilde{\lambda}, t)$, where $\mathcal{M}_{\mathcal{R}} \equiv \mathcal{M}_{\Omega}(\tilde{\lambda} \rightarrow +\infty)$ is the total seawater mass in the region $\mathcal{R}$. Similarly, intermediate water masses are defined by $\mathcal{M}_{\Omega}(\tilde{\lambda}_1; \tilde{\lambda}_2) \equiv \int_{\tilde{\lambda}_1 < \lambda' \leq \tilde{\lambda}_2} \rho \, \mathrm{d}V = \mathcal{M}_{\Omega}(\tilde{\lambda}_2) - \mathcal{M}_{\Omega}(\tilde{\lambda}_1)$.

To understand the evolution of $M_{\Omega}(\tilde{\lambda}, t)$ over time, we start by integrating the seawater mass conservation equation,

$$\frac{\partial \rho}{\partial t} = -\boldsymbol{\nabla} \cdot (\rho \boldsymbol{v}), \tag{3}$$

over the spatial extent of the water mass $\Omega(\tilde{\lambda}, t)$. Invoking the divergence theorem, we have

$$\int\limits_{\Omega(\tilde{\lambda},t)} \frac{\partial \rho}{\partial t} \, \mathrm{d}V = - \int\limits_{\Omega(\tilde{\lambda},t)} \boldsymbol{\nabla} \cdot (\rho \boldsymbol{v}) \, \mathrm{d}V = - \oint\limits_{\partial\Omega(\tilde{\lambda},t)} \rho \boldsymbol{v} \cdot \hat{\boldsymbol{n}} \, \mathrm{d}S, \tag{4}$$

where we define $\partial\Omega$ as the surface that bounds Ω and $\hat{\boldsymbol{n}}$ is the outward normal unit vector. Since the water mass $\Omega(\tilde{\lambda}, t)$ is time-varying, time derivatives do not commute with the density-weighted volume integral:

$$\frac{\partial}{\partial t} \mathcal{M}_{\Omega}(\tilde{\lambda}, t) \equiv \frac{\partial}{\partial t} \int\limits_{\Omega(\tilde{\lambda},t)} \rho \, \mathrm{d}V \neq \int\limits_{\Omega(\tilde{\lambda},t)} \frac{\partial \rho}{\partial t} \, \mathrm{d}V. \tag{5}$$

Hence, we cannot simply pull the time derivative on the left-hand side (LHS) of equation (4) out of the volume integral. Instead, we must invoke the three-dimensional generalization of Leibniz' integral rule (also known as Leibniz-Reynolds' transport theorem), which accounts for the time-evolving bounds of integration through an additional term:

$$\frac{\partial}{\partial t} \int\limits_{\Omega(\tilde{\lambda},t)} F \, \mathrm{d}V = \int\limits_{\Omega(\tilde{\lambda},t)} \frac{\partial F}{\partial t} \, \mathrm{d}V + \oint\limits_{\partial\Omega(\tilde{\lambda},t)} F \, \boldsymbol{v}^{(\partial\Omega)} \cdot \hat{\boldsymbol{n}} \, \mathrm{d}S, \tag{6}$$

where $F(\boldsymbol{x}, t)$ is an arbitrary scalar function and $\boldsymbol{v}^{(\partial\Omega)}$ is the velocity of the boundary $\partial\Omega$ itself. A nonzero boundary velocity $\boldsymbol{v}^{(\partial\Omega)}$ can occur as a result of movement in either the bounding $\tilde{\lambda}$-isosurface or the boundaries of the region $\mathcal{R}$. The boundary velocity is generally decoupled from the fluid velocity; the important exception is for a material region that follows the flow, in which

$$\boldsymbol{v}^{(\partial\Omega)} \cdot \hat{\boldsymbol{n}} = \boldsymbol{v} \cdot \hat{\boldsymbol{n}} \quad \text{(material region)}. \tag{7}$$

Applying equation (6) to the case of $F = \rho$ and combining with equation (4), we find that λ-water mass evolution is determined by a balance between flow convergence within the water mass and the movement of the water mass' boundary:

$$\frac{\partial}{\partial t}\mathcal{M}_{\Omega}(\tilde{\lambda}, t) \equiv \frac{\partial}{\partial t} \int\limits_{\Omega(\tilde{\lambda},t)} \rho \, \mathrm{d}V = - \oint\limits_{\partial\Omega(\tilde{\lambda},t)} \rho \, (\boldsymbol{v} - \boldsymbol{v}^{(\partial\Omega)}) \cdot \hat{\boldsymbol{n}} \, \mathrm{d}S. \tag{8}$$

This form of equation (8) is useful because the surface integral can be evaluated separately for each of the different categories of the water mass boundary, $\partial\Omega$.

2.2 Characterizing dia-surface transport and boundary conditions

For an arbitrary region $\mathcal{R}$ of the ocean (e.g., Figure 1), we consider four distinct categories of water mass boundaries: the sea floor, the sea surface, interior λ-isosurfaces, and any remaining boundaries of $\mathcal{R}$ that do not fall under one of the other categories. We can thus evaluate the total surface integral by considering the disjoint union

$$\partial\Omega(\tilde{\lambda}, t) \equiv \partial\Omega_{\text{seafloor}}(\tilde{\lambda}, t) \sqcup \partial\Omega_{\text{surf}}(\tilde{\lambda}, t) \sqcup \mathcal{A}_{\mathcal{R}}(\tilde{\lambda}, t) \sqcup \partial\mathcal{R}. \tag{9}$$

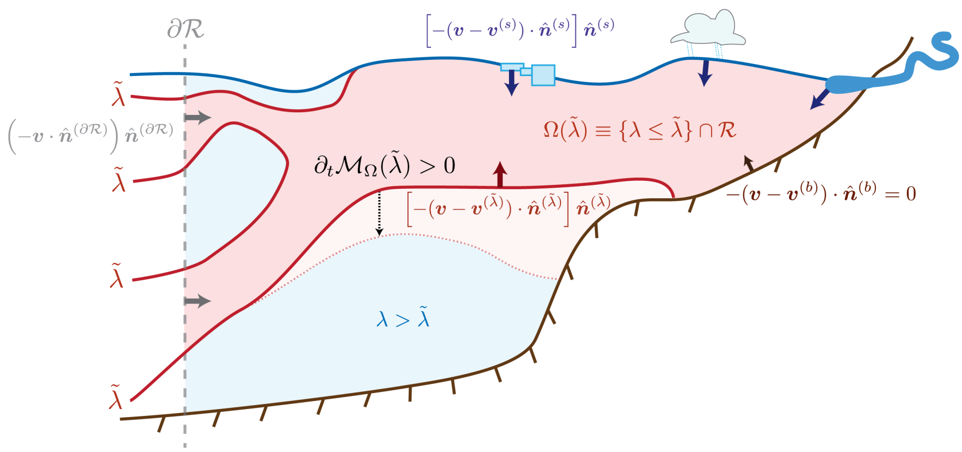

Figure 1. A schematic (x, z) profile view of the λ-water mass budget (equation (8)) for a water mass $\Omega(\tilde{\lambda}, t)$ defined by the region $\mathcal{R}$ and tracer values that satisfy $\lambda(\boldsymbol{x}, t) \leq \tilde{\lambda}$ for a specific choice of $\tilde{\lambda}$. Note that λ is not required to be monotonic with depth and it is possible for multiple isosurfaces of λ to exist within a single vertical profile. The water mass $\Omega(\tilde{\lambda}, t)$ is bounded by the seafloor (brown), sea surface (blue), interior λ-isosurfaces (red), and a specifed regional boundary $\partial\mathcal{R}$ (grey dashed). Water mass changes are due to mass fluxes across each of these boundaries, except the impermeable seafloor.

Boundary 1: the seafloor. The seafloor is assumed to be static ($\boldsymbol{v}^{(b)} = 0$), trivially leading to $\rho \, \boldsymbol{v}^{(b)} \cdot \hat{\boldsymbol{n}}^{(b)} = 0$. It is also impermeable to fluid flow, so that $\rho \, \boldsymbol{v} \cdot \hat{\boldsymbol{n}}^{(b)} = 0$.

Boundary 2: the sea surface. The sea surface, on the other hand, is time dependent and permeable, allowing for exchanges of mass due to processes like precipitation, evaporation, sea ice freezing/melting, river inflow, etc. Following section 4 of A. G. Nurser and Griffies (2019), this transport condition is given by

$$\rho \, (\boldsymbol{v} - \boldsymbol{v}^{(s)}) \cdot \hat{\boldsymbol{n}}^{(s)} = -\mathcal{Q}_{\mathrm{M}}^{\mathrm{surf}}, \tag{10}$$

where $\mathcal{Q}_{\mathrm{M}}^{\mathrm{surf}}$ is the net mass flux crossing the boundary per unit surface area due to the various exchange processes mentioned above. We thus define the net surface mass flux into the water mass as

$$\mathcal{S}_{\Omega}(\tilde{\lambda}, t) \equiv - \int\limits_{\partial\Omega_{\mathrm{surf}}(\tilde{\lambda},t)} \rho\, (\boldsymbol{v} - \boldsymbol{v}^{(s)}) \cdot \hat{\boldsymbol{n}}^{(s)}\, \mathrm{d}S = \int\limits_{\partial\Omega_{\mathrm{surf}}(\tilde{\lambda},t)} \mathcal{Q}_{\mathrm{M}}^{\mathrm{surf}} \mathrm{d}S. \tag{11}$$

In practice, it is more convenient to work in terms of the horizontal projection of $\mathrm{d}S$, which we write as $\mathrm{d}A$, and thus define the normalized surface mass flux

$$Q_{\mathrm{M}}^{\mathrm{surf}} \equiv \mathcal{Q}_{\mathrm{M}}^{\mathrm{surf}}\, \mathrm{d}S/\mathrm{d}A, \tag{12}$$

which we use hereafter.

Boundary 3: interior $\tilde{\lambda}$-isosurfaces. This surface is the boundary between the regions in $\mathcal{R}$ where $\lambda < \tilde{\lambda}$ and $\lambda > \tilde{\lambda}$, with normal vector $\hat{\boldsymbol{n}}^{(\tilde{\lambda})} = \nabla\lambda/|\nabla\lambda|$. Note that, so long as λ is continuous, $|\nabla\lambda| > 0$ on the $\tilde{\lambda}$-isosurface. We defer the further treatment of this case to Section 2.3, where we relate the density-weighted dia-$\tilde{\lambda}$ velocity, $(\boldsymbol{v} - \boldsymbol{v}^{(\tilde{\lambda})}) \cdot \hat{\boldsymbol{n}}^{(\tilde{\lambda})}$, to the kinematic material time derivative that appears in the λ conservation equation (16). The density-weighted dia-$\tilde{\lambda}$ velocity is then integrated along the $\lambda = \tilde{\lambda}$ isosurface, $\mathcal{A}_{\mathcal{R}}(\tilde{\lambda}, t)$, which we again emphasize need not be contiguous or single-valued in a water column.

Boundary 4: specified regional boundaries. Finally, the velocities of (and across) the remaining surfaces of $\partial\Omega(\tilde{\lambda}, t)$ depend on the definition of the specified region of interest, $\mathcal{R}(t)$. When $\mathcal{R}$ is the global ocean, for example, the other three boundaries already constitute all of $\partial\Omega$ and this term vanishes. Another useful limit is when $\mathcal{R}$ is time-independent, such that $\boldsymbol{v}^{(\partial\mathcal{R})} = 0$, and we only need consider the contribution from the cross-boundary flow, $\boldsymbol{v}\cdot\hat{\boldsymbol{n}}^{(\partial\mathcal{R})}$. A further simplifying assumption, which has been adopted in most prior regional water mass transformation analyses (including Groeskamp et al. (2019) and Bailey et al. (2023)) and will be employed hereafter, is that the region has vertical boundaries. In this case, $\hat{\boldsymbol{z}}\cdot\hat{\boldsymbol{n}}^{(\partial\mathcal{R})} = 0$ such that $\boldsymbol{v}\cdot\hat{\boldsymbol{n}}^{(\partial\mathcal{R})}$ depends only on the horizontal velocity

$$\boldsymbol{u} \equiv (\boldsymbol{v} \cdot \hat{\boldsymbol{x}})\, \hat{\boldsymbol{x}} + (\boldsymbol{v} \cdot \hat{\boldsymbol{y}})\, \hat{\boldsymbol{y}}. \tag{13}$$

We define the net convergent horizontal mass transport across the region's boundaries $\partial\mathcal{R}$ (see Figure 1) as

$$\Psi_{\partial\mathcal{R}}(\tilde{\lambda}, t) \equiv - \int\limits_{\partial\mathcal{R}\,\cap\,\{\lambda\leq\tilde{\lambda}\}} \rho\, \boldsymbol{u} \cdot \hat{\boldsymbol{n}}^{(\partial\mathcal{R})}\, \mathrm{d}S, \tag{14}$$

where the surface integral includes the vertical boundaries of the region, where $\lambda \leq \tilde{\lambda}$.

Altogether, the λ-water mass budget equation (8) within the region $\mathcal{R}$ can thus be written as

$$\frac{\partial}{\partial t}\mathcal{M}_{\Omega}(\tilde{\lambda}, t) = \mathcal{S}_{\Omega}(\tilde{\lambda}, t) - \int\limits_{\mathcal{A}_{\mathcal{R}}(\tilde{\lambda},t)} \rho(\boldsymbol{v} - \boldsymbol{v}^{(\tilde{\lambda})}) \cdot \hat{\boldsymbol{n}}^{(\tilde{\lambda})}\, \mathrm{d}S + \Psi_{\partial\mathcal{R}}(\tilde{\lambda}, t). \tag{15}$$

While equation (15) is conceptually straightforward, the surface integral appearing on the right-hand side (RHS) is unwieldy and challenging to diagnose from both observation and models; we derive a more tractable expression for it in the following section.

2.3 Dia-$\tilde{\lambda}$ transport and water mass transformation

The natural starting point for developing a better understanding of the drivers of dia-$\tilde{\lambda}$ transport is the conservation equation for the tracer concentration λ,

$$\frac{\mathrm{D}\lambda}{\mathrm{D}t} \equiv \frac{\partial\lambda}{\partial t} + \boldsymbol{v} \cdot \boldsymbol{\nabla}\lambda = \dot{\lambda}, \tag{16}$$

where $\frac{\mathrm{D}}{\mathrm{D}t}$ is the material time derivative (which is the total time derivative computed following the fluid flow) and $\dot{\lambda}$ represents the sum of all processes that modify or transform the λ concentration along that trajectory. Example processes leading to transformation include boundary exchange fluxes, molecular (or parameterized turbulent) diffusion, and internal tracer sources or sinks (e.g. chemical reactions, ecological species interactions, or radioactive decay). Multiplying equation (16) by $\rho/|\boldsymbol{\nabla}\lambda|$ and integrating along the $\lambda = \tilde{\lambda}$ isosurface within $\mathcal{R}$, denoted $\mathcal{A}_{\mathcal{R}}(\tilde{\lambda}, t)$, we arrive at

$$\int\limits_{\mathcal{A}_{\mathcal{R}}(\tilde{\lambda},t)} \frac{\rho}{|\boldsymbol{\nabla}\lambda|}\frac{\partial\lambda}{\partial t}\,\mathrm{d}S + \int\limits_{\mathcal{A}_{\mathcal{R}}(\tilde{\lambda},t)} \rho\,\boldsymbol{v}\cdot\frac{\boldsymbol{\nabla}\lambda}{|\boldsymbol{\nabla}\lambda|}\,\mathrm{d}S = \int\limits_{\mathcal{A}_{\mathcal{R}}(\tilde{\lambda},t)} \frac{\rho\,\dot{\lambda}}{|\boldsymbol{\nabla}\lambda|}\,\mathrm{d}S. \tag{17}$$

Dividing by $|\boldsymbol{\nabla}\lambda|$ requires that it not vanish anywhere along the $\tilde{\lambda}$-isosurface $\mathcal{A}_{\mathcal{R}}(\tilde{\lambda}, t)$; while this may at first seem like a stringent constraint, however, it will always be the case so long as λ is continuous. Note that it is perfectly fine for one or two components of the gradient to vanish, as in the case of vertical overturns, but the three-dimensional gradient will not vanish on any point on the surface as this would imply the point ceases to be on the boundary between where $\lambda < \tilde{\lambda}$ and $\lambda > \tilde{\lambda}$, which is the definition of the isosurface. In the second term on the LHS of the isosurface-integrated equation (17), we recognize $\hat{\boldsymbol{n}}^{(\tilde{\lambda})} \equiv \boldsymbol{\nabla}\lambda/|\boldsymbol{\nabla}\lambda|$ as the unit vector normal to the $\tilde{\lambda}$-isosurface, thus identifying this term with the flow-velocity component of the dia-surface transport term that appears in the mass budget equation (15),

$$\int\limits_{\mathcal{A}_{\mathcal{R}}(\tilde{\lambda},t)} \rho\,\boldsymbol{v}\cdot\frac{\boldsymbol{\nabla}\lambda}{|\boldsymbol{\nabla}\lambda|}\,\mathrm{d}S = \int\limits_{\mathcal{A}_{\mathcal{R}}(\tilde{\lambda},t)} \rho\,\boldsymbol{v}\cdot\boldsymbol{n}^{(\tilde{\lambda})}\,\mathrm{d}S. \tag{18}$$

The boundary-velocity component of the dia-$\tilde{\lambda}$ transport term is instead defined kinematically as the velocity $\boldsymbol{v}^{(\lambda)}$ along which λ is materially conserved,

$$\frac{\partial\lambda}{\partial t} + \boldsymbol{v}^{(\lambda)}\cdot\boldsymbol{\nabla}\lambda = 0. \tag{19}$$

Again assuming $|\boldsymbol{\nabla}\lambda| \neq 0$, equation (19) can be multiplied by $\rho/\boldsymbol{\nabla}\lambda$ and rearranged as

$$\rho\,\boldsymbol{v}^{(\lambda)}\cdot\hat{\boldsymbol{n}}^{(\lambda)} = -\frac{\rho}{|\boldsymbol{\nabla}\lambda|}\frac{\partial\lambda}{\partial t}. \tag{20}$$

Substituting equations (18) and (20) into equation (17), we can re-express the dia-$\tilde{\lambda}$ mass transport in terms of isosurface-integrated λ-tendencies, evaluated along the particular $\lambda = \tilde{\lambda}$ isosurface,

$$\int\limits_{\mathcal{A}_{\mathcal{R}}(\tilde{\lambda},t)} \rho(\boldsymbol{v} - \boldsymbol{v}^{(\tilde{\lambda})})\cdot\hat{\boldsymbol{n}}^{(\tilde{\lambda})}\,\mathrm{d}S = \int\limits_{\mathcal{A}_{\mathcal{R}}(\tilde{\lambda},t)} \rho\frac{\left(\frac{\partial\lambda}{\partial t} + \boldsymbol{v}\cdot\boldsymbol{\nabla}\lambda\right)}{|\boldsymbol{\nabla}\lambda|}\,\mathrm{d}S = \int\limits_{\mathcal{A}_{\mathcal{R}}(\tilde{\lambda},t)} \frac{\rho\dot{\lambda}}{|\boldsymbol{\nabla}\lambda|}\,\mathrm{d}S. \tag{21}$$

To make evaluation of the surface integrals in equation (21) more amenable to our anticipated finite-volume discretization, we reformulate the definition of λ-water masses as integrals in λ coordinates. Applying the chain rule, we first re-express the dia-λ thickness, $\mathrm{d}h$, of an infinitesimal volume element $\mathrm{d}V$ in λ coordinates, $\mathrm{d}\lambda = |\boldsymbol{\nabla}\lambda|\,\mathrm{d}h$, such that $\mathrm{d}V = \mathrm{d}h\mathrm{d}S = \mathrm{d}\lambda\mathrm{d}S/|\boldsymbol{\nabla}\lambda|$. We can re-express the density-weighted integral of an arbitrary scalar function $\mathcal{F}(\boldsymbol{x}, t)$ over the water mass $\Omega(\tilde{\lambda}, t)$ as

$$G_{\Omega}^{(\mathcal{F})}(\tilde{\lambda}, t) \equiv \int\limits_{\Omega(\tilde{\lambda},t)} \rho\,\mathcal{F}\,\mathrm{d}V = \int\limits_{-\infty}^{\tilde{\lambda}} \left[\ \oint\limits_{\mathcal{A}_{\mathcal{R}}(\tilde{\lambda}',t)} \rho\,\mathcal{F}\,\mathrm{d}S\right]\mathrm{d}h = \int\limits_{-\infty}^{\tilde{\lambda}} \left[\ \oint\limits_{\mathcal{A}_{\mathcal{R}}(\tilde{\lambda}',t)} \frac{\rho\,\mathcal{F}}{|\boldsymbol{\nabla}\lambda|}\,\mathrm{d}S\right]\mathrm{d}\tilde{\lambda}', \tag{22}$$

where we emphasize that $\partial\Omega(\tilde{\lambda}, t)$ is the full boundary of the water mass while $\mathcal{A}_{\mathcal{R}}(\tilde{\lambda}, t)$ is just the $\tilde{\lambda}$-isosurface and excludes the lateral boundary $\partial\mathcal{R}$ and the seafloor. Taking the partial derivative with respect to $\tilde{\lambda}$ and applying the Fundamental Theorem of Calculus, we have the generalized *dia-$\tilde{\lambda}$ transformation relation* for the arbitrary scalar $\mathcal{F}$,

$$\mathcal{G}_{\Omega}^{(\mathcal{F})}(\tilde{\lambda}, t) \equiv \partial_{\tilde{\lambda}} G_{\Omega}^{(\mathcal{F})} = \partial_{\tilde{\lambda}} \left[\int\limits_{\Omega(\tilde{\lambda},t)} \rho\, \mathcal{F}\, \mathrm{d}V \right] = \oint\limits_{\mathcal{A}_{\mathcal{R}}(\tilde{\lambda},t)} \frac{\rho\, \mathcal{F}}{|\boldsymbol{\nabla}\lambda|}\, \mathrm{d}S. \tag{23}$$

In doing so, we have ignored the contribution from the lower bound ($\tilde{\lambda}' \rightarrow -\infty$) because $\int_{\mathcal{A}_{\mathcal{R}}(\tilde{\lambda}',t)} \frac{\rho \mathcal{F}}{|\boldsymbol{\nabla}\lambda|}\, \mathrm{d}S \rightarrow 0$ as $\tilde{\lambda}'$ decreases below the range of realizable values and thus the area $\mathcal{A}_{\mathcal{R}}(\tilde{\lambda}', t)$ of the isosurface vanishes; in practice, it suffices to set a lower limit of $\tilde{\lambda}_0 < \min\{\lambda(\boldsymbol{x}, t)\}$.

Taking the arbitrary scalar $\mathcal{F}$ to be λ-tendencies, the dia-$\tilde{\lambda}$ transformation relation (23) allows us to express the surface integrals in equation (21) as volume integrals. First, we integrate the density-weighted λ conservation equation (17) over $\Omega(\tilde{\lambda}, t)$ and take a derivative with respect to $\tilde{\lambda}$:

$$\underbrace{\frac{\partial}{\partial\tilde{\lambda}} \left[\int\limits_{\Omega(\tilde{\lambda},t)} \rho\, \frac{\partial \lambda'}{\partial t}\, \mathrm{d}V \right]}_{\mathcal{G}_{\Omega}^{(\partial_t)}(\tilde{\lambda},t)} + \underbrace{\frac{\partial}{\partial\tilde{\lambda}} \left[\int\limits_{\Omega(\tilde{\lambda},t)} \rho\, (\boldsymbol{v} \cdot \boldsymbol{\nabla}\lambda')\, \mathrm{d}V \right]}_{\mathcal{G}_{\Omega}^{(\mathrm{A})}(\tilde{\lambda},t)} = \underbrace{\frac{\partial}{\partial\tilde{\lambda}} \left[\int\limits_{\Omega(\tilde{\lambda},t)} \rho\, \dot{\lambda}'\, \mathrm{d}V \right]}_{\mathcal{G}_{\Omega}^{(\mathrm{T})}(\tilde{\lambda},t)}. \tag{24}$$

We refer to equation (24) as the λ-*Water Mass Transformation* (λ-WMT) equation because the dia-$\tilde{\lambda}$ transformation relation (23) allows us to then combine equations (21) and (24), yielding an expression for the dia-$\tilde{\lambda}$ transport in terms of differential λ-transformation tendencies integrated over the water mass (see definition on RHS of equation 24),

$$\int\limits_{\mathcal{A}_{\mathcal{R}}(\tilde{\lambda},t)} \rho(\boldsymbol{v} - \boldsymbol{v}^{(\tilde{\lambda})}) \cdot \hat{\boldsymbol{n}}^{(\tilde{\lambda})}\, \mathrm{d}S = \mathcal{G}_{\Omega}^{(\mathrm{T})}(\tilde{\lambda}, t), \tag{25}$$

which we simply refer to as the total *water mass transformation.* The terms in equations (24) and (25) have units of mass transport, kg/s; motivated by the Boussinesq approximation, they can be converted into equivalent volume transports (units of m^3/s or $\mathrm{Sv} \equiv 10^6\,\mathrm{m}^3/\mathrm{s}$) by dividing by a reference density such as $\rho_0 \approx 1035\,\mathrm{kg/m}^3$.

Now that we have defined our final expressions for each term, we drop the variables' arguments for conciseness. It is often useful to decompose the transformation term by process type (Figure 2), e.g.,

$$\mathcal{G}_{\Omega}^{(\mathrm{T})} \equiv \mathcal{G}_{\Omega}^{(\mathrm{Surface})} + \mathcal{G}_{\Omega}^{(\mathrm{Ice\text{-}Ocean})} + \mathcal{G}_{\Omega}^{(\mathrm{Seafloor})} + \mathcal{G}_{\Omega}^{(\mathrm{Mix})}, \tag{26}$$

or even more granularly by physical process (e.g., brine rejection, radiative cooling, diapycnal mixing by internal wave breaking, isopycnal mixing by mesoscale eddies). To simplify discussions of the λ-water mass budgets diagnosed from our Baltic Sea simulation, we hereafter bundle all fluxes across external ocean boundaries into:

$$\mathcal{G}_{\Omega}^{(\mathrm{BF})} \equiv \mathcal{G}_{\Omega}^{(\mathrm{Surface})} + \mathcal{G}_{\Omega}^{(\mathrm{Ice\text{-}Ocean})} + \mathcal{G}_{\Omega}^{(\mathrm{Seafloor})}. \tag{27}$$

2.4 The λ-Water Mass Transformation Budget

The power of the λ-water mass budget approach arises when we replace the total surface integral in the λ-water mass budget equation (8) with our expressions for the nonzero mass transports across the sea surface (11), interior $\tilde{\lambda}$-isosurfaces (25), and lateral boundaries (14), yielding the concise λ-WMT budget:

$$\partial_t \mathcal{M}_{\Omega} = \mathcal{S}_{\Omega} - \mathcal{G}_{\Omega}^{(\mathrm{T})} + \Psi_{\partial\mathcal{R}}. \tag{28}$$

Rearranging equation (28) as

$$\partial_t \mathcal{M}_\Omega - \mathcal{S}_\Omega - \Psi_{\partial\mathcal{R}} = -\mathcal{G}_\Omega^{(\mathrm{T})} \tag{29}$$

clarifies the distinction between the *kinematic mass budget terms* on the LHS and the *water mass transformation processes* on the RHS. In the context of numerical ocean models, equation (29) is not necessarily closed because additional *spurious* water mass transformations $\mathcal{G}_\Omega^{(\mathrm{S})}$ can arise due to discretization errors; we defter a detailed investigation of spurious nuermical mixing until Section 3.5. The λ-WMT budget is illustrated schematically in Figure 2.

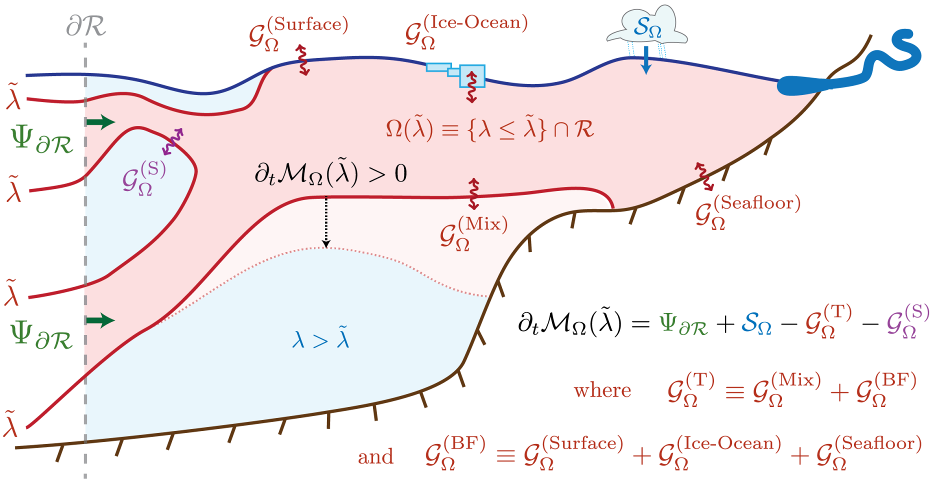

Figure 2. A schematic (x, z) profile view of the λ-WMT budget (equation (41)) for a water mass $\Omega(\tilde{\lambda}, t)$ defined by the region $\mathcal{R}$ and tracer values that satisfy $\lambda(\boldsymbol{x}, t) \leq \tilde{\lambda}$ for a specific choice of $\tilde{\lambda}$. Note that λ is not required to be monotonic with depth and it is possible for multiple isosurfaces of λ to exist within a single vertical profile. The water mass $\Omega(\tilde{\lambda}, t)$ is bounded by the seafloor (brown), sea surface (blue), interior λ-isosurfaces (red), and a specifed regional boundary $\partial\mathcal{R}$ (grey dashed). The various terms in the budget are defined throughout Section 2. The dia-scalar transformation term $\mathcal{G}_\Omega^{(\mathrm{T})}$ is decomposed into the contributions from fluxes across the sea surface, seafloor, and λ-isosurface. An additional term $\mathcal{G}_\Omega^{(\mathrm{S})}$ is introduced to account for water mass transformations associated with spurious numerical mixing (see Section 3.5).

2.5 Example: Water Mass Transformations in the Baltic Sea

Example evaluations of the λ-WMT budget equation (29) are shown in Figure 3 for $\lambda = \Theta$ (Conservative Temperature), S (Absolute Salinity), and ρ_0 (potential density referenced to atmospheric pressure) in a region $\mathcal{R}$ of the inner Baltic Sea (whose boundary $\partial\mathcal{R}$ is visualized later in Figures 5 and 9). The region contains two distinct water masses (Figure 3a): (1) light fresh water of seasonally-varying temperature in the shallow inner Baltic Sea and (2) salty, cold, and dense open ocean water at the entrance to the Baltic Sea. Let us consider the dominant features of this region's annual-mean WMT budgets.

In temperature space (Figure 3b), a leading-order balance emerges between surface heat fluxes (which warm warm water and cool cold water) and interior mixing (which mixes cold and warm waters together, transforming both towards intermediate temperatures). Interestingly, near 2.5 °C, the warming of cold waters due to mixing is not balanced by surface cooling, resulting in a small annual mean drift towards warmer water classes. In salinity space (Figure 3c), we see two distinct lobes of water mass transformation, consistent with the bimodal water mass distribution seen in Figure 3a. For the deep water lobe with S $>$ 20 ppt, interior mixing again produces a straightforward dipole structure as relatively fresh (S $<$ 29 ppt) and salty ($>$ 29 ppt) waters are mixed together; however, only the fresh part of these mixing-driven transformations are balanced by surface flux salinification, with the freshening of the salty part instead being primarily balanced by a net export of relatively fresh water into the open ocean. The WMT budget in potential density space (Figure 3d) closely follows that of salinity, except for the lightest waters ($\rho_0 < 1007\,\mathrm{kg/m^3}$) where the temperature-related transformations are concentrated.

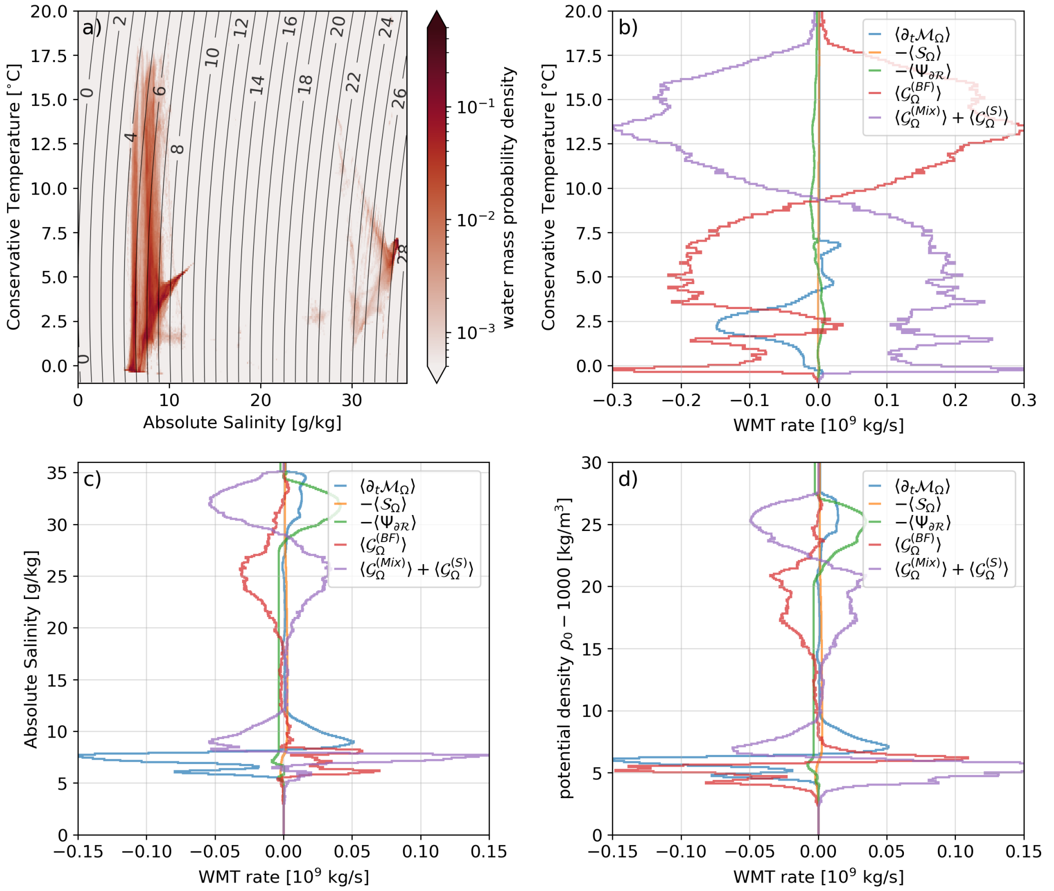

Figure 3. Examples of water masses and their budgets for the region $\mathcal{R}$ of the Baltic Sea shown in Figure 9. a) The distribution of water masses in $\mathcal{R}$ as a function of Conservative Temperature, Absolute Salinity, and potential density $\rho_0 - 1000\,\mathrm{kg/m^3}$ (referenced to atmospheric pressure, shown as black contours) averaged over a full year, mainly provided as context for the budgets that follow. b-d) Annual-mean (angle brackets) WMT budgets (eq. 29) in Conservative Temperature, Absolute Salinity, and potential density coordinates, diagnosed as described in Section 3 but using timestep-averaged diagnostics in the model's native prognostic vertical coordinate to minimize discretization errors. Total water mass transformations $\mathcal{G}_\Omega^{(\mathrm{T})}$ are broken down into two components: boundary fluxes $\mathcal{G}_\Omega^{(\mathrm{BF})}$ and mixing, which includes both directly diagnosed parameterized mixing $\mathcal{G}_\Omega^{(\mathrm{Mix})}$ and spurious numerical mixing $\mathcal{G}_\Omega^{(\mathrm{S})}$, which we identify as the remainder of the other budget terms (see Section 3.5). With in-situ densities of $\rho \approx 1000\,\mathrm{kg/s}$, a water mass transformation rate of $10^9\mathrm{kg/s}$ is approximately equivalent to $1\,\mathrm{Sv} \equiv 10^6\mathrm{m^3/s}$.

2.6 On steady-state λ-Water Mass Transformation Budgets

Assuming a steady-state (i.e. $\boldsymbol{v}^{(\tilde{\lambda})} = 0$) and neglecting the typically small surface mass flux term (i.e. $\mathcal{S}_\Omega = 0$), the WMT budget equations (15 and 29) reduce to:

$$\Psi_{\partial\mathcal{R}} = \int\limits_{\mathcal{A}_\mathcal{R}(\tilde{\lambda})} \rho \boldsymbol{v} \cdot \hat{\boldsymbol{n}}^{(\tilde{\lambda})} \mathrm{d}S = \mathcal{G}_\Omega^{(\mathrm{T})}. \tag{30}$$

We remind the reader that the area $\mathcal{A}_\mathcal{R}(\tilde{\lambda})$ of the $\tilde{\lambda}$-isosurface within $\mathcal{R}$ is the subset of the total water mass boundary $\partial\Omega$ that excludes the lateral boundary $\partial\mathcal{R}$, the sea surface, and the seafloor. Equation (30) states that the convergent horizontal circulation into a region is exactly balanced by the circulation across its bounding $\tilde{\lambda}$-isosurface, which is driven by the sum of the water mass transformation processes. A common application of water mass transformation theory is to use an estimate of the RHS of the steady-state equation (30) in density coordinates to infer the diapycnal overturning circulation it induces on the LHS (e.g. de Lavergne et al., 2016; Ferrari et al., 2016; Drake et al., 2020). Marsh et al. (2000) warn, however, about the dangers of incorrectly applying the steady state equation (30) to an unsteady meridional overturning circulation. Testing the steady-state assumption in the context of our annual-mean S-WMT budgets in the Baltic Sea (Figure 4), we find that the assumption is fairly reasonable for salty waters (in the deep open ocean), but not the fresh waters (in the shallow inner Baltic Sea) which are drifting at leading order (Figure 3c).

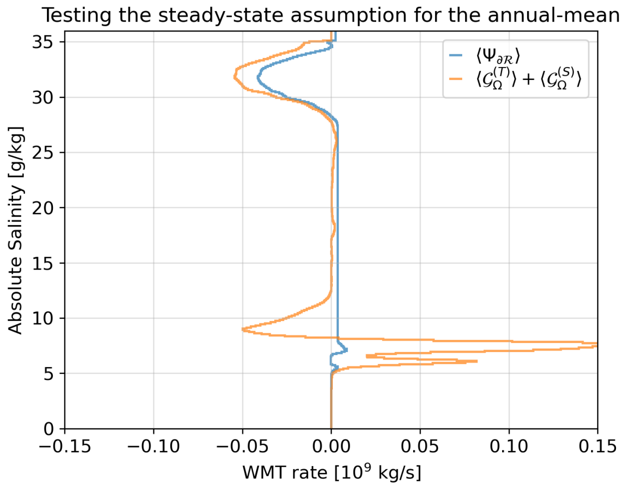

Figure 4. A test of the steady-state S-WMT budget assumption (eq. 30), reproducing Figure 3c except that we have now bundled all of the transformation terms together, including both directly diagnosed transformations $\mathcal{G}_\Omega^{(\mathrm{T})} = \mathcal{G}_\Omega^{(\mathrm{BF})} + \mathcal{G}_\Omega^{(\mathrm{Mix})}$ and spurious transformations $\mathcal{G}_\Omega^{(\mathrm{S})}$ (see Section 3.5) and have changed the sign of the transport term for more direct comparison.

3 Diagnosing Discretized λ-Water Mass Transformation Budgets

In this section, we adapt the continuous theory outlined above to express the WMT budget in a form befitting the diagnostic output provided by numerical ocean models. We would like to diagnose the terms in the time-mean WMT budget (29), given by

$$\langle \partial_t \mathcal{M}_\Omega \rangle - \langle \mathcal{S}_\Omega \rangle - \langle \Psi_{\partial\mathcal{R}} \rangle + \langle \mathcal{G}_\Omega^{(\mathrm{T})} \rangle = 0 \tag{31}$$

where

$$\langle \phi \rangle \equiv \frac{1}{\Delta t} \int_{t_n}^{t_n + \Delta t} \phi \, \mathrm{d}t \tag{32}$$

is the diagnostic time-averaging operator over a given interval of length Δt and centered around $t_{n+\frac{1}{2}}$. For clarity, we assume *a priori* that all diagnostics have been conservatively regridded and remapped into λ bins $[\lambda_{m-\frac{1}{2}}, \lambda_{m+\frac{1}{2}}]$ (denoting layer m), where overbars $\overline{\phi}^m$ denote layer averages. We emphasize that whatever vertical regridding/remapping scheme is employed, it should be conservative so that total water mass and tracer content is conserved. Any any case, results should be robust to changes in the diagnostic and target grids (see Section 3.6). We will use i and j as horizontal grid indices (with a straightforward extension to adjacency matrices for unstructured mesh implementations, e.g. Ringler et al. (2013)) and q as the λ layer index. We discuss aliasing errors due to 'offline' remapping with time-mean diagnostics in Section 3.6.

3.1 Kinematic mass tendency

The Fundamental Theorem of Calculus allows us to write the time-mean mass tendency term as the difference between snapshots bounding the averaging interval,

$$\langle \partial_t \mathcal{M}_\Omega \rangle = (\Delta t)^{-1} [\mathcal{M}_\Omega]_{t_n}^{t_n + \Delta t}. \tag{33}$$

For a given interface $\tilde{\lambda} = \lambda_{m+\frac{1}{2}}$, each of these mass snapshots can be estimated by cumulatively summing layer masses, $h_q \, \overline{\rho}^q \, \mathrm{d}A$, for all layers with $\lambda_q \leq \lambda_{m+\frac{1}{2}}$ within a tracer cell mask R that approximates the continuous region $\mathcal{R}$,

$$\langle \partial_t \mathcal{M}_\Omega \rangle (\lambda_{m+\frac{1}{2}}, t_{n+\frac{1}{2}}) \simeq \frac{1}{\Delta t} \left[\sum_{i,j \in \mathrm{R}} \sum_{q < m+\frac{1}{2}} h_q \, \overline{\rho}^q \, \mathrm{d}A \right]_{t_n}^{t_n + \Delta t}. \tag{34}$$

3.2 Convergent horizontal mass transport

The transport term, $\langle \Psi_\Omega \rangle$, requires accumulating all mass transports normal to the region's boundary, $\partial \mathcal{R}$, with a consistently convergent orientation, for $\lambda \leq \tilde{\lambda}$. Since the surface integral form of this term originates from the divergence theorem, internal consistency of the discretized mass budget requires that the discrete boundary, $\partial \mathrm{R} \approx \partial \mathcal{R}$, exactly follow the faces of the finite volume elements that bound the tracer cell mask, R, as illustrated in Figure 5. The total convergent transport across ∂R is computed by summing the convergent mass transports over all layers with $\lambda_q \leq \lambda_{m+\frac{1}{2}}$ and over all of the cell faces along the boundary ∂R:

$$\langle \Psi_{\partial \mathcal{R}} \rangle (\lambda_{m+\frac{1}{2}}, t_{n+\frac{1}{2}}) \equiv \left\langle \int_{\partial \mathcal{R} \cap \{\lambda \leq \lambda_{m+\frac{1}{2}}\}} -\rho \, \boldsymbol{u} \cdot \hat{\boldsymbol{n}}^{(\partial \mathcal{R})} \, \mathrm{d}A \right\rangle \simeq \sum_{i^{(\boldsymbol{u})}, j^{(\boldsymbol{u})} \in \partial \mathrm{R}} \left[\sum_{\lambda_q \leq \lambda_{m+\frac{1}{2}}} (-\overline{\rho \, \boldsymbol{u}}^q \, h_q \, \mathrm{d}\ell) \cdot \hat{\boldsymbol{n}}^{(\partial \mathrm{R})} \right], \tag{35}$$

where $i^{(\boldsymbol{u})}, j^{(\boldsymbol{u})}$ are the grid face indices that correspond to the normal mass fluxes $\left[(\rho \boldsymbol{u}) \cdot \hat{\boldsymbol{n}}^{(\partial \mathcal{R})}\right] \hat{\boldsymbol{n}}^{(\partial \mathcal{R})}$ and $\mathrm{d}\ell$ are the widths of grid cell faces. Since local recirculations can be orders of magnitude larger than the net convergence into a region (Figure 5, inset arrows), inexact interpolation methods (e.g. for a boundary ∂R that does not exactly follow the grid cell faces bounding the mask R) or seemingly minor indexing errors can balloon into leading-order errors in the overall WMT budget and therefore corrupt the identification of the residual as spurious numerical mixing.

Our method for directly computing boundary-normal convergent transports, which consists of finding pairs of grid face indices $(i^{(\boldsymbol{u})}, j^{(\boldsymbol{u})})$ and assigning the appropriate sign for the inward orientation $-(\overline{\rho \, \boldsymbol{u}}^q \, h_q \, \mathrm{d}\ell) \cdot \hat{\boldsymbol{n}}^{(\partial \mathrm{R})}$, is illustrated in Figure 5 and briefly described in Appendix D. We have verified for various definitions of discrete boundaries

$\mathrm{R} \approx \mathcal{R}$ that the surface integral of the convergent mass flux along $\partial\mathrm{R}$ is within machine precision of the volume-integrated convergent mass flux diagnostic within R, thereby satisfying the divergence theorem on the model grid.

An alternative method of diagnosing the convergent horizontal mass transport into the discrete region R is to first compute the convergence into each individual grid column C (where $\mathrm{R} = \bigcup\{\mathrm{C}\}$), and then sum the convergent transport over all of the columns in R to get the net convergent transport,

$$\langle \Psi_{\partial\mathcal{R}} \rangle (\lambda_{m+\frac{1}{2}}, t_{n+\frac{1}{2}}) \simeq \sum_{\mathrm{C}\subseteq\mathrm{R}} \left\{ \sum_{i^{(\boldsymbol{u})}, j^{(\boldsymbol{u})} \in \partial\mathrm{C}} \left[\sum_{\lambda_q \leq \lambda_{m+\frac{1}{2}}} (\overline{\rho \boldsymbol{u}^q}\, h_q\, \mathrm{d}\ell) \cdot \hat{\boldsymbol{n}}^{(\partial\mathrm{C})} \right] \right\}. \tag{36}$$

[We use this approach to diagnose the maps of column-wise horizontal mass transport convergence shown in Figure 9c, discussed in detail later in the text]. Benefits of computing the convergence of horizontal mass transports for each grid column individually are: 1) it is readily diagnosed from the finite difference of horizontal mass transports across the lateral faces of a grid column, significantly simplifying its implementation; 2) it is positioned at the center of tracer grid cells, allowing it to be conveniently integrated with all of the other diagnostics required to close the λ-WMT budget; 3) it can be precomputed once globally and then efficiently reused for various choices of R; and 4) it enables column-wise estimation of spurious numerical mixing (see Section 3.5 and Holmes et al. (2021)), rather than a single bulk estimate for the entire region R. A major disadvantage of this column-wise approach, however, is that it provides no information about the spatial structure of normal mass transports along the boundary $\partial\mathrm{R}$ (as shown in Figure 5), which may be necessary information for some applications. Our software packages described in Appendix D allow users to specify either of these two methods to calculate the transport convergence term.

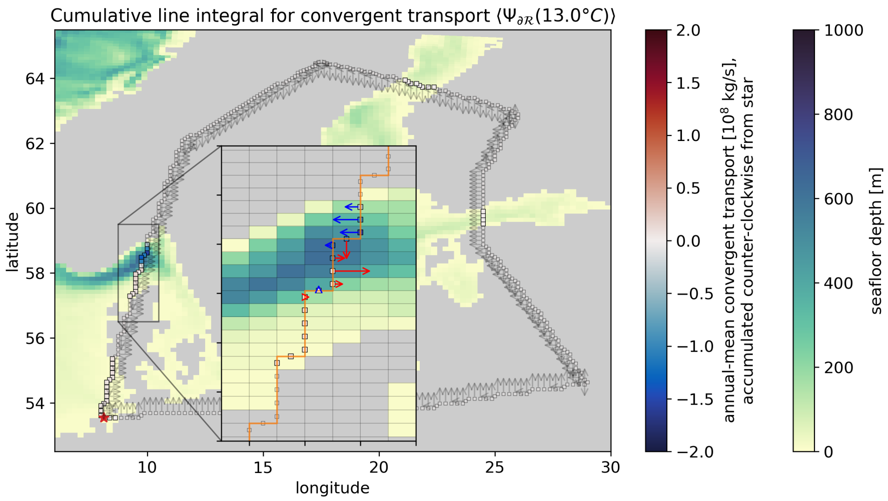

Figure 5. Annual-mean convergent transport (expression 36 diagnosed as 35) into the discrete region R, integrated for waters colder than $\Theta = 13\,^\circ$C, as a counterclockwise cumulative line integral beginning from the red star. The black arrows show the orientation of the inward-facing normal vectors $-\hat{\boldsymbol{n}}^{(\partial\mathrm{R})}$ for each grid face along the discrete boundary $\partial\mathrm{R}$. The inset zooms in on the entrance to the Baltic Sea, where the net mass transport is the relatively small residual of fluxes in (red arrows) and out (blue arrows) of the region; for clarity, we only show the handful of arrows that correspond to transports larger than 10% of the maximum cross-boundary transport.

3.3 Boundary mass source

The boundary mass source term,

$$\langle \mathcal{S}_\Omega \rangle(\lambda_{m+\frac{1}{2}}, t_{n+\frac{1}{2}}) = \left\langle \int\limits_{\partial\Omega_{\text{surf}}} Q_M^{\text{surf}} \, \mathrm{d}A \right\rangle, \tag{37}$$

is estimated by simply summing $Q_M^{\text{surf}} \, \mathrm{d}A$ for all $\lambda_q^{\text{surf}} \leq \lambda_{m+\frac{1}{2}}$. This term is globally small but can be important in smaller regions with large and concentrated freshwater fluxes (e.g. major river inflows or rapidly melting sea ice, icebergs, or ice shelves).

3.4 Transformation rates

Water mass transformation terms $\mathcal{G}_\Omega^{(\star)}$, i.e. those in the form of the λ-Water Mass Transformation equation (24), are approximated by finite difference:

$$\mathcal{G}_\Omega^{(\mathrm{T})} \equiv \frac{\partial}{\partial \tilde{\lambda}} \int\limits_{\Omega(\tilde{\lambda},t)} \rho \, \dot{\lambda} \, \mathrm{d}V \simeq \frac{\int_{\Omega(\lambda_{m+\frac{1}{2}})} \rho \, \dot{\lambda} \, \mathrm{d}V - \int_{\Omega(\lambda_{m-\frac{1}{2}})} \rho \, \dot{\lambda} \, \mathrm{d}V}{\lambda_{m+\frac{1}{2}} - \lambda_{m-\frac{1}{2}}} \tag{38}$$

where $\rho \, \dot{\lambda} \, \mathrm{d}V$ represents tracer mass tendencies arising from material transformation processes. In the Riemann sum evaluation of the integral, these tendencies take the form of the density-weighted and layer-integrated tracer tendency terms shown in equations (A34)–(A35) (derived in Appendix A), as scaled by the vertically-uniform area element $\mathrm{d}A$.

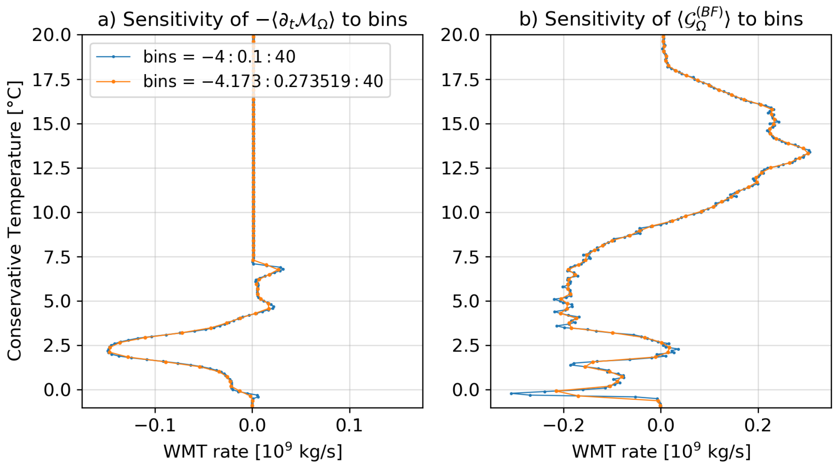

Figure 6. Sensitivity of the Θ-WMT budget to the choice of λ bins for (a) the mass tendency term and (b) the boundary flux transformation rate term (eq. 27). Both terms are integrated over the discrete region mask R shown in Figure 5. Blue curves show the default bins (every 0.1 °C, from −4 °C to 40 °C) and orange curves show the same terms recalculated with alternative bins that are larger than, and offset from, the default. Differences between the two calculations are much smaller than the resolved features of interest, giving us confidence that discretization errors in our offline diagnostic methods are negligible.

Water mass transformation rates can be inherently noisy, making it difficult to distinguish actual process-based variability from methodological errors. A robust method for assessing whether variability is due to diagnostic discretization errors is to assess the results' sensitivity to the choice of the target $\tilde{\lambda}$ bins. For three-dimensional general circulation models and $\mathcal{O}(100)$ target bins, it is common for each target bin to represent thousands of grid cells and thus for the results to be relatively robust. Regions of exceptionally strong or weak gradients, $|\nabla\lambda|$, however, may require more careful considerations of the target $\tilde{\lambda}$ grid. Our experience is that sensitivity to binning is sufficiently small to not affect interpretation of results (see Figure 6), except perhaps for small regions consisting of just a few grid columns. Noise at the grid column level was a major motivation for Holmes et al. (2021)'s diathermal transport approach, which essentially amounts to smoothing out the noise in the Θ-WMT budget equation by integrating in $\tilde{\Theta}$.

3.5 Spurious numerical mixing

Theoretically, the time-averaged λ-WMT budget (31) should exactly hold (with the minor caveat that, strictly speaking, this also requires $|\nabla\lambda| \neq 0$ along the $\tilde{\lambda}$-isosurface). In practice, however, discretization errors in the advection schemes used in ocean models can induce water mass transformations in excess of those resulting from the imposed or parameterized material transformation processes, $\rho\dot{\lambda}$. To build intuition about spurious mixing, consider the limiting case in which $\mathcal{R}$ is global, such that $\langle\Psi_{\partial\mathcal{R}}\rangle = 0$, and there are no prescribed mass fluxes or material tracer tendencies, i.e. $\mathcal{S}_\Omega = 0$ and $\dot{\lambda} = 0$ (such that $\mathcal{G}^{(\mathrm{T})}_\Omega = 0$), respectively. In theory, equation (29) should then reduce to $\partial_t\mathcal{M}_\Omega = 0$, meaning the λ-water mass distribution should remain exactly as is. [Note that the steadiness of the λ-water mass distribution does not impose any restrictions on the steadiness of the flow or tracer fields, which can in principle still be quite turbulent and variable– as in the adiabatic eddying simulations of Marques et al. (2022), with $\lambda = \rho_2$]. Most advection schemes employed in ocean models result in errors that are dispersive and/or diffusive in nature, which in λ-space manifest as spurious water mass transformations, i.e. $\partial_t\mathcal{M}_\Omega(\tilde{\lambda}, t) \neq 0$. This point applies even to semi-Lagrangian FV-GVC models in which the vertical coordinate σ is λ itself (e.g. density transformations in a density coordinate model), since such approaches must rely on imperfect vertical regridding/remapping schemes to accomodate interior dia-σ transports. Purely isopycnal coordinate models (e.g. stacked shallow water models) are spared from spurious diapycnal mixing by construction, but are subject to other problems that limit their viability for global climate modeling (Fox-Kemper et al., 2019).

In the general case, spurious numerical water mass transformations $\mathcal{G}^{(\mathrm{S})}_\Omega(\tilde{\lambda}, t)$ can be identified as the remainder of the λ-WMT budget equation (29),

$$\mathcal{G}^{(\mathrm{S})}_\Omega \equiv [-(\partial_t\mathcal{M}_\Omega - \mathcal{S}_\Omega - \Psi_{\partial\mathcal{R}})] - \mathcal{G}^{(\mathrm{T})}_\Omega \neq 0, \tag{39}$$

where the sign convention is chosen to match those of the other material water mass transformation terms, for example allowing transformations due to parameterized and spurious mixing to be directly compared. We emphasize that the remainder $\mathcal{G}^{(\mathrm{S})}_\Omega$ can be nonzero even if both the mass and tracer conservation equations are themselves closed in every grid cell, because spurious dia-$\tilde{\lambda}$ transformations may be embedded within the diagnosed advective λ tendency. Crucially, closure of cell-wise tracer budgets does not imply closure of λ-WMT budgets or that spurious mixing is vanishingly small!

Because we have already accounted for all non-advective WMTs when subtracting $\mathcal{G}^{(\mathrm{T})}_\Omega$ in equation (39), the remaining spurious numerical errors can only be due to errors in the tracer advection operator. [An interpretive limitation of this approach is that we are unable to distinguish between spurious WMTs due to horizontal vs. vertical aspects of advection schemes.] It is useful to interpret the transformations $\mathcal{G}^{(\mathrm{A})}_\Omega$ diagnosed from the advective tracer tendency in equation (24) as the difference of two distinct components:

$$\mathcal{G}^{(\mathrm{A})}_\Omega \equiv \mathcal{G}^{(\mathrm{D})}_\Omega - \mathcal{G}^{(\mathrm{S})}_\Omega, \tag{40}$$

where $-\mathcal{G}^{(\mathrm{S})}_\Omega$ represents transformations due to spurious numerical mixing (diagnosed following eq. 39, with its arbitrary sign chosen to match that of the other material WMT terms) and we identify $\mathcal{G}_\Omega^{(\mathrm{D})}$ as the yet unknown diascalar mass transport induced by all material transformation (including spurious numerical mixing). Since $\mathcal{G}_\Omega^{(\mathrm{A})}$ is directly diagnosed from the discrete advective tracer operator, we can also indirectly diagnose the sum $\mathcal{G}_\Omega^{(\mathrm{D})} = \mathcal{G}_\Omega^{(\mathrm{A})} + \mathcal{G}_\Omega^{(\mathrm{S})}$.

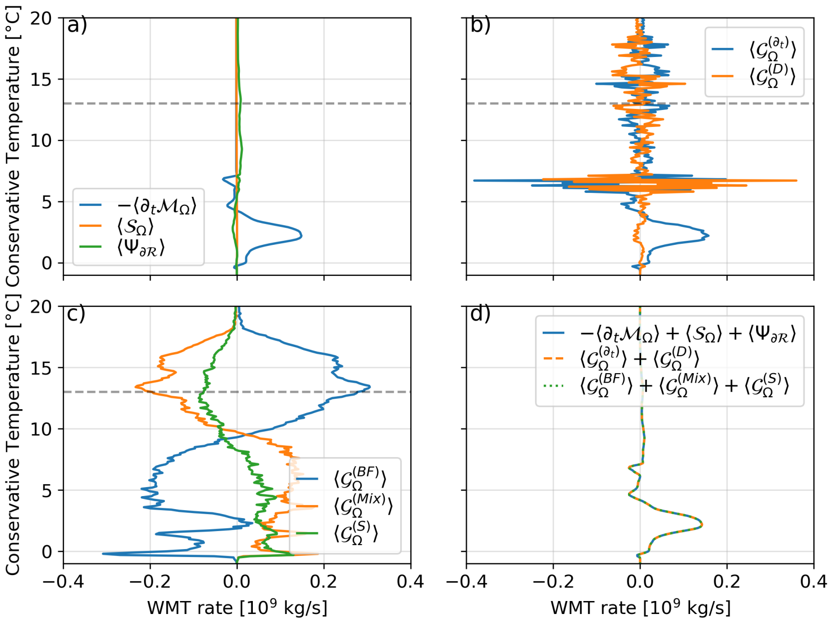

Figure 7. Three equivalent ways of decomposing material water mass transformations (equation 41; panel d) in Conservative Temperature coordinates ($\lambda = \Theta$): a) The terms of the kinematic transformation rate; b) the dia-surface transformation rate (which include strongly compensating bin-scale features); and c) the process-based transformation rate, which includes contributions from spurious numerical mixing $\mathcal{G}_\Omega^{(\mathrm{S})}$ and for which we further decompose the transformation term (following eq. (26)) into boundary flux and interior mixing contributions, $\mathcal{G}_\Omega^{(\mathrm{T})} = \mathcal{G}_\Omega^{(\mathrm{BF})} + \mathcal{G}_\Omega^{(\mathrm{Mix})}$. d) Demonstration that all three decompositions are exactly equivalent, which is true by construction because $\mathcal{G}_\Omega^{(\mathrm{S})}$ and $\mathcal{G}_\Omega^{(\mathrm{D})}$ are both diagnosed as remainders of the other terms. The inner Baltic Sea region of integration R, is shown in Figure 5. Figure 9 shows the local grid-column contributions to the three key terms for $\Theta = 13\,°\mathrm{C}$ (dashed grey line).

Combining the definitions (39) and (40) with the water mass transformation equation (24), we identify three equivalent and complementary perspectives for interpreting water mass change in FV-GVC ocean models:

$$\underbrace{-\partial_t \mathcal{M}_\Omega + \mathcal{S}_\Omega + \Psi_{\partial \mathcal{R}}}_{\substack{\text{Kinematic}\\ \text{transformation}}} = \underbrace{\mathcal{G}_\Omega^{(\partial_t)} + \mathcal{G}_\Omega^{(\mathrm{D})}}_{\substack{\text{Dia-surface}\\ \text{transformation}}} = \underbrace{\mathcal{G}_\Omega^{(\mathrm{T})} + \mathcal{G}_\Omega^{(\mathrm{S})}}_{\substack{\text{Material property}\\ \text{transformation}}} . \tag{41}$$

The three decompositions of WMT defined by equation 41 are shown in Figure 7. Figure 7c shows that spurious numerical mixing plays a large enough role in the budget to be non-negligible; its temperature structure closely follows that of parameterized mixing, but with just 20-50% of its magnitude. Like physical (parameterized turbulent) diffusion, spurious water mass transformations conserve tracer mass and thus are compensatory in nature, such that the destruction of one water mass is exactly balanced by the formation of another.

Rearranging equation (7) and decomposing the diagnosed material transformations into the components due to boundary fluxes and interior mixing, $\mathcal{G}_\Omega^{(\mathrm{T})} = \mathcal{G}_\Omega^{(\mathrm{BF})} + \mathcal{G}_\Omega^{(\mathrm{Mix})}$, we arrive at the closed λ-WMT budget,

$$\partial_t \mathcal{M}_\Omega - \mathcal{S}_\Omega - \Psi_{\partial\mathcal{R}} + \mathcal{G}_\Omega^{(\mathrm{BF})} + \mathcal{G}_\Omega^{(\mathrm{Mix})} + \mathcal{G}_\Omega^{(\mathrm{S})} = 0. \tag{42}$$

Figure 8 shows that even when integrated over the many grid columns that comprise the inner Baltic region, the Θ-WMT budget is highly variable with time. The given isotherm $\tilde{\Theta} = 13\,^\circ\mathrm{C}$ only exists in the Baltic region R during the summer, so during the rest of the year the water mass Ω covers the entire region ($\Omega = \mathcal{R}$) and all of the terms in the WMT budget are vanishingly small. During the summer, the budget is dominated by the diurnal formation and destruction of cold water masses by boundary heat fluxes (Figure 8a). Smoothing over the diurnal cycle, we find that surface heating steadily transforms cold waters into warmer ones, although this process is partially opposed by parameterized mixing with cold waters (Figure 8b). By contrast, in the fall surface fluxes and mixing conspire to form cold waters. WMTs due to spurious numerical mixing are generally near-zero, but exhibit some short-lived negative excursions that contribute to an overall transformation towards lower temperatures–reinforcing the effects of parameterized mixing (Figure 8b). Further smoothing clarifies the annual-mean balance in the WMT budget (Figure 8c): net heating by surface fluxes is balanced by parameterized and numerical mixing; direct mass fluxes and lateral mass transports into the region are both negligible.

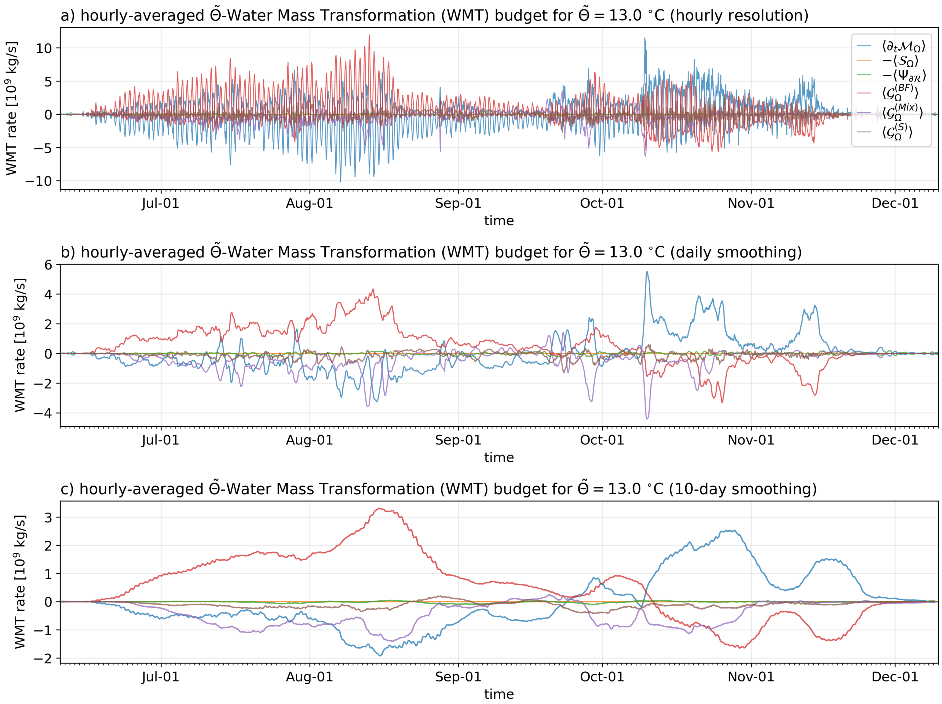

Figure 8. Contributions to the Θ-WMT budget (eq. 42) integrated over the inner Baltic region, for $\Theta = 13\,^\circ\mathrm{C}$. The hourly (timestep)-averaged budget (a) is dominated by the diurnal cycle, so we also show the results of daily box-averaging (b) and 10-day box-averaging (c).

It can also be insightful to analyze maps of local (per unit area) WMT rates (e.g. Maze et al., 2009; Drake et al., 2020; Holmes et al., 2021). Figure 9 shows the annual-mean column-wise WMT budget for waters colder than $\tilde{\Theta} = 13\,^\circ\mathrm{C}$ in the Baltic region

R. The annual-mean mass tendency is small (Figure 9a) because waters warmer than 13 °C only exist in the summer and the total mass of water columns in the inner Baltic does not change much from year to year. The dominant column-wise balance is between the warming effect of surface heat fluxes and the cooling effect of parameterized mixing, consistent with the region-wide integral. Column-wise lateral mass transport convergence and transformations due to spurious numerical mixing are both relatively noisy (Figure 9a). While the noisy lateral convergent transports average out to near-zero (Figure 8), the noisy transformations due to spurious numerical mixing are overwhelmingly negative, and contribute to the overall cooling of the water mass.

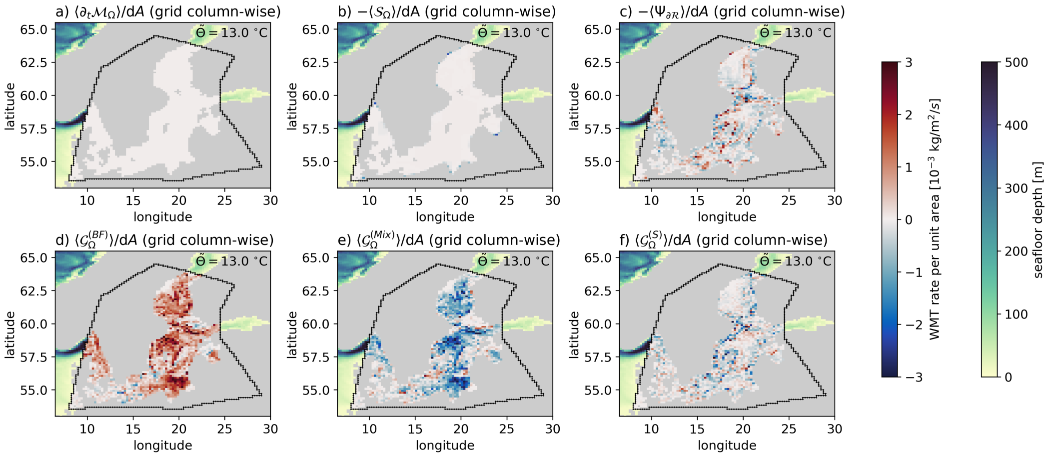

Figure 9. Column-wise contributions to the annual-mean Θ-WMT budget (eq. 42) by term in the inner Baltic region, for $\Theta = 13$ °C. Each panel shows the summand of the corresponding discretized diagnostics described in Section 3, divided by the grid column area dA. The region $\mathcal{R}$ is a spherical polygon defined here by the coordinates of eight user-provided vertices, where the black contour shows the discretized boundary ∂R that best approximates the continuous boundary $\partial\mathcal{R}$ as a sequence of model grid faces.

3.6 Offline vertical remapping and temporal aliasing errors

Thus far we have assumed that the required diagnostics are available in λ coordinates (i.e. were remapped online to a diagnostic grid before time-averaging the outputs). In practice, however, one must often make do with diagnostics that are only available on other vertical coordinate grids, such as depth levels, isopycnals, terrain-following coordinates, or other GVCs. Problematically, the time-averaging operator, $\langle\phi\rangle$, does not commute with vertical remapping if layer-integrated λ-tendencies and λ values covary on timescales shorter than the averaging interval. Remapping interval-averaged tracer diagnostics to tracer coordinates thereby introduces errors in the WMT budget.

In our year-long Baltic Sea test configuration at 0.25° horizontal grid spacing, we quantify these errors by brute-force, comparing calculations with diagnostic averaging intervals that decrease from monthly, to daily, and finally all the way down to the hourly model timestep. First, we consider the sensitivity of the ρ_2-WMT budget to the diagnostic averaging interval and the choice of vertical coordinate (Figure 10); because ρ_2 is available as an 'online' diagnostic coordinate in our MOM6 simulations, ρ_2-WMT budgets are independent of the diagnostic averaging interval (compare Figure 10c,f,i) and therefore serve as a ground truth against which we can compare our offline calculations. The convergence of the offline depth-level and prognostic hybrid coordinate budgets to-

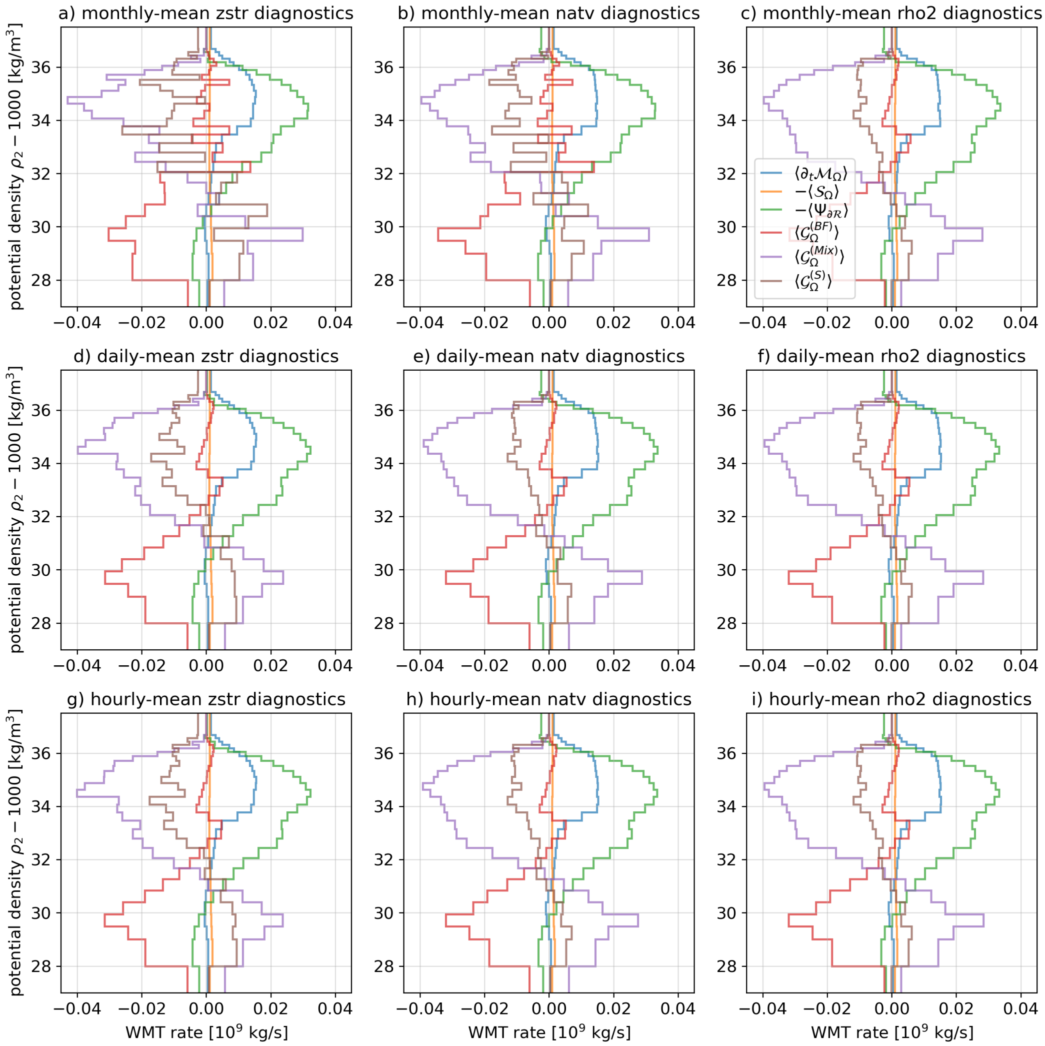

Figure 10. Sensitivity of annual-mean ρ_2-WMT budgets to the diagnostic averaging interval Δt (rows) and the diagnostic vertical coordinate (columns), where `zstr` denotes depth-levels, `natv` denotes prognostic hybrid coordinate levels, and `rho2` denotes potential density surfaces referenced to 2000 dbar. Diagnostics in non-`rho2` coordinates are transformed into the bins of the `rho2` diagnostic to facilitate direct comparison. Because the `rho2` diagnostics are already binned in ρ_2 coordinates online, the WMT budgets for `rho2` are independent of the averaging interval. The non-`rho2` diagnostics converge towards the `rho2` diagnostic results to varying degrees as the averaging interval is reduced; the rate of change and overturning terms are particularly well represented even with monthly-averaged diagnostics.

wards the online density coordinate budget (compare 10a-c to d-f to g-i) demonstrates that monthly-averaged diagnostics introduce significant errors while daily-mean diagnostics are nearly indistinguishable from those with the hourly-mean/timestep diagnostics. Even with the timestep-averaged diagnostics, however, there are still noticeable errors in the `zstr` diagnostics; this is likely because the effective resolution of the `zstr` diagnostic coordinate differs substantially from that of the `natv` and `rho2` diagnostic coordinates.

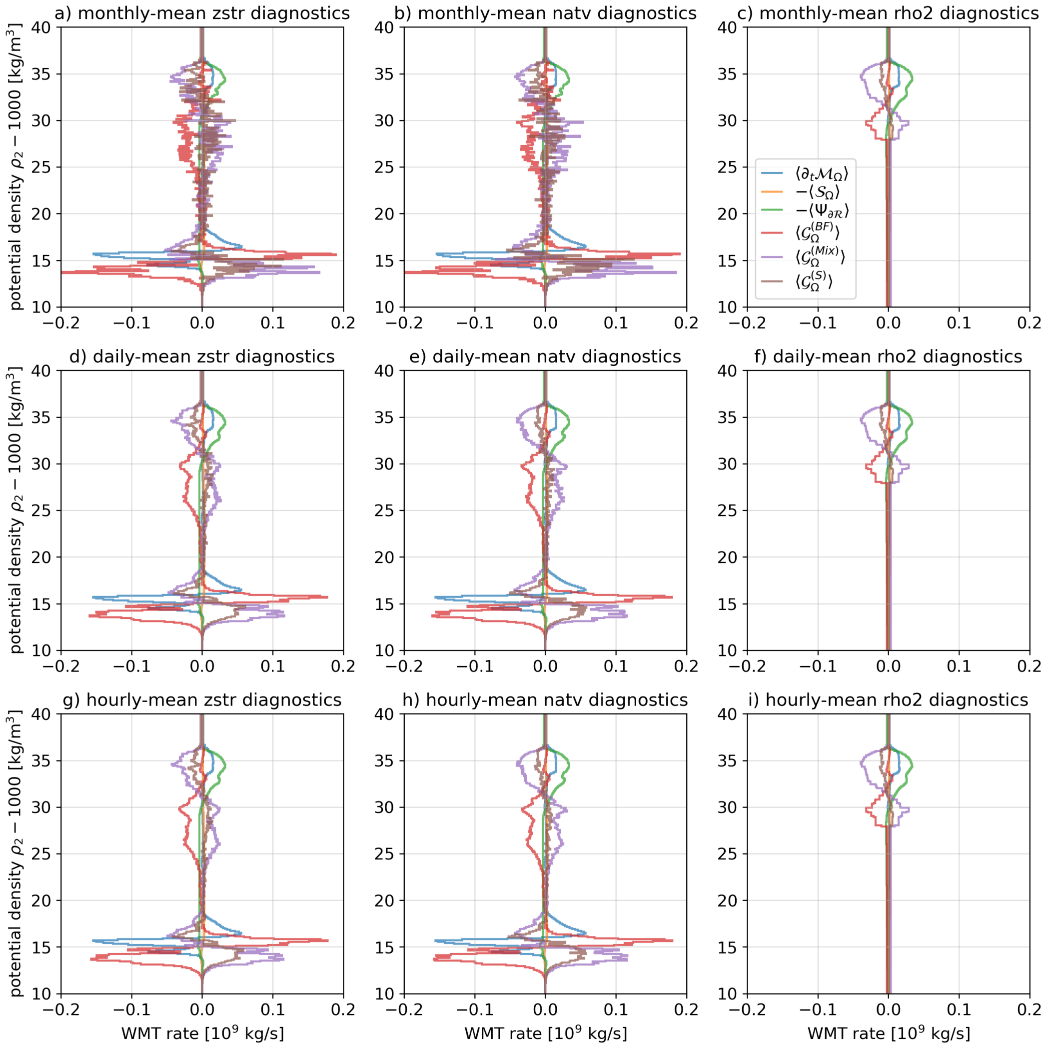

Figure 11. Sensitivity of annual-mean ρ_2-WMT budgets to the diagnostic averaging interval Δt (rows) and the diagnostic vertical coordinate (columns), where `zstr` denotes depth-levels, `natv` denotes prognostic hybrid coordinate levels, and `rho2` denotes potential density surfaces referenced to 2000 dbar. Diagnostics in all three coordinates are transformed into a common target $\tilde{\rho}_2$ grid with uniformly fine spacing of $\Delta\tilde{\rho}_2 = 0.1\,\mathrm{kg/m}^3$. Because the `rho2` diagnostics are already binned in $\tilde{\rho}_2$ coordinates online, the WMT budgets for `rho2` are independent of the averaging interval; however, the relatively coarse bins of the $\tilde{\rho}_2$ grid used for the online diagnostics (see bin limits in Figure 10) obscures interesting finer-scale features of the ρ_2-WMT budget (compare panels g and h to i).

616 Next, we repeat our calculation of the ρ_2-WMT budget but now use a target $\tilde{\rho}_2$ grid that differs significantly from the online diagnostic grid (Figure 11), in particular by making the $\tilde{\rho}_2$ bin spacing much finer at lower densities. As before, the calculations employing monthly-mean depth-level and hybrid coordinate diagnostics are fairly noisy but converge reasonably well when dropped to daily-means. Again, the ρ_2 calculations remain by construction independent of the averaging interval; however, comparison with the brute-forced calculations using hourly-mean diagnostics in depth-level and prognostic hybrid coordinates (Figure 11g-i) reveals that the online-binning in $\tilde{\rho}_2$ coordinates

obscures interesting leading-order features at scales finer than the diagnostic $\tilde{\rho}_2$ grid, and which can not be recovered.

Finally, we repeat the same exercise but for a Θ-WMT budget. Because Conservative Temperature Θ was not yet available as an online diagnostic coordinate in MOM6, all three sets of diagnostics were transformed into Θ coordinates offline. From the top row of Figure 12, we observe that offline calculations with monthly-mean diagnostics are noisy, while those with daily-mean diagnostics are quite similar to the hourly-mean/timestep ones. Interestingly, the density-coordinate calculations differ substantially from those with the depth-level and prognostic hybrid coordinates, which are themselves in agreement. These errors appear to be due to the very low effective resolution of the density-coordinate grid in the shallow and fresh inner Baltic Sea (see Figures 3 and 11), meaning the whole water column is in some cases represented by a single density layer, over which the Θ values and Θ-tendency diagnostics are then averaged.

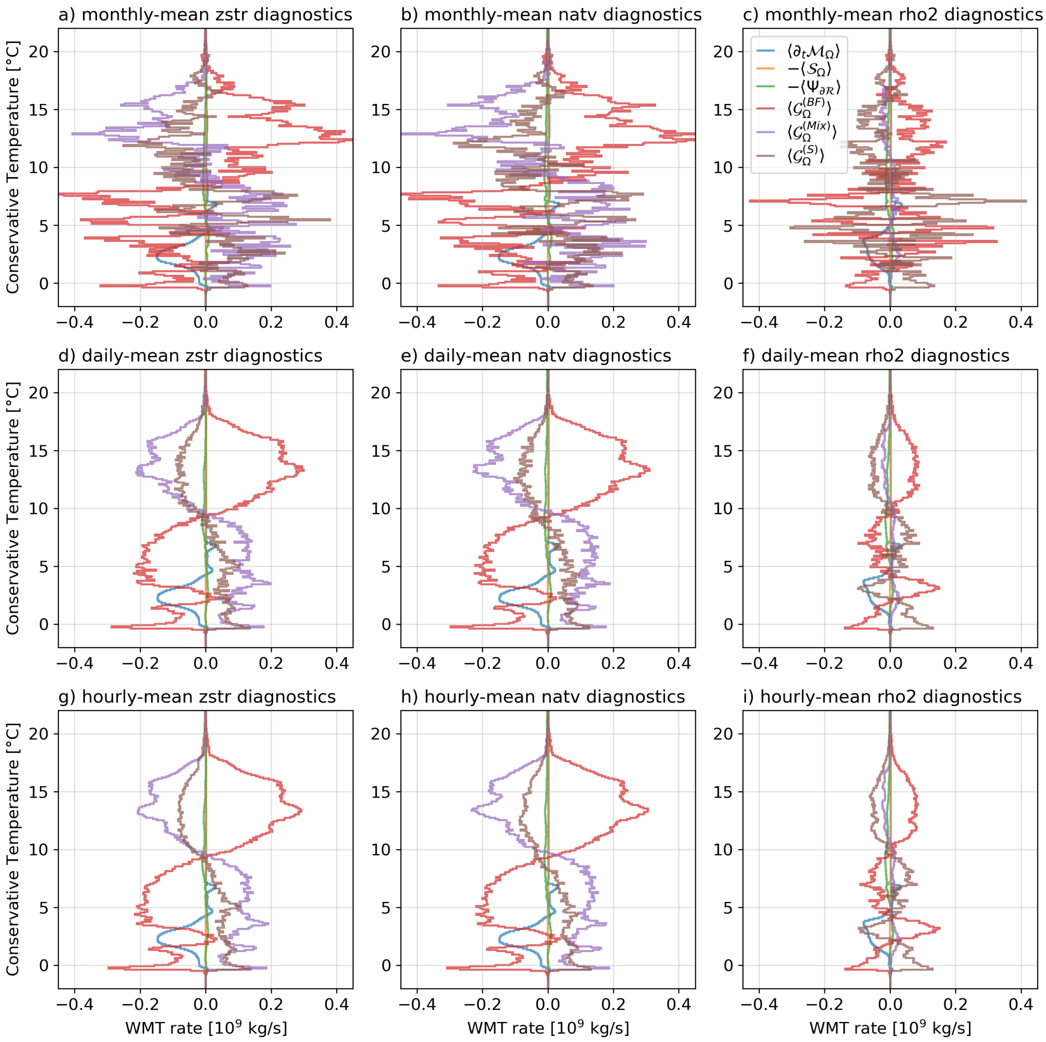

Figure 12. Sensitivity of annual-mean Θ-WMT budgets to the diagnostic averaging interval Δt (rows) and the diagnostic vertical coordinate (columns), where `zstr` denotes depth-levels, `natv` denotes prognostic hybrid coordinate levels, and `rho2` denotes potential density surfaces referenced to 2000 dbar. The `rho2` diagnostics do not converge to the correct values because most of the Baltic Sea occupies the single lightest layer of the diagnostic potential density grid.

For most ocean model applications, outputting thousands of three-dimensional tendency fields with an averaging interval shorter than the inherent variability of the model is resource-intensive and largely untenable. Instead, it is recommended that all required diagnostics be conservatively regridded and remapped online into $\tilde{\lambda}$ coordinate bins after each tracer timestep, so that longer-term time-averaged diagnostics can be meaningfully accumulated (at the cost of slower model run times) and more readily analyzed. Such online remapping of diagnostics was recommended as part of the OMIP exercise by Griffies et al. (2016), with this technology becoming more standard across ocean climate model codes. However, the leading-order differences between the various λ-WMT budgets described above (Figures 10-12) serve as a caution that one should carefully tune their diagnostic coordinates to the problem at hand to avoid the risk of ending up with noisy or misleading WMT budgets. (In the case of the Baltic Sea simulation described here, the employed diagnostic $\tilde{\rho}_2$ grid was previously calibrated to capture features of the Meridional Overturning Circulation in global climate model configurations, so it is not surprising that it poorly resolves water masses in the marginal Baltic Sea.)

4 Outlook

As Water Mass Transformation (WMT) analysis becomes an increasingly popular tool for advancing understanding of ocean circulation (Tesdal et al., 2023; Evans et al., 2023) and coupled climate dynamics (Deppenmeier et al., 2022), it is all the more important that the methods used to diagnose terms in WMT budgets be correct and that the scientific interpretations of these results be robust. We intend for this self-contained presentation of the theory and practice of diagnosing WMT budgets to be a useful reference for practitioners of water mass analysis, especially (but not only) as applied to numerical ocean models. We contend that full WMT budgets are an under-utilized tool in the ocean and climate modeler's toolbox, with applications to both model development (e.g., identifying the processes causing water mass biases, circulation biases, and unwanted spurious mixing and control model drift) and scientific discovery (e.g., attributing the drivers of variability and change in water mass properties and overturning circulations).

The method for diagnosing λ-WMT budgets presented here requires the scalar field λ to satisfy a conservation equation of the form (16) and that the diagnostics for each of the terms in the conservation budget be available, as described in Appendix A. This is generally true for prognostic tracers, i.e. tracers that are time-stepped within a FV-GVC ocean model, such as temperature, salinity, and biogeochemical tracers. Diagnostic tracers, which are instead derived from the prognostic tracers using algebraic equations or elliptic partial differential equations, however, do not necessarily satisfy exact conservation equations of the form required for water mass transformation analysis.

Seawater *in-situ* density, ρ, is an example of a more complicated diagnostic tracer, as it depends nonlinearly on temperature, salinity, and pressure (T. McDougall et al., 2009). Because gravity acts upon seawater density gradients, it would be advantageous to analyze oceanic flows along surfaces over which this buoyancy force vanishes, i.e., *neutral surfaces*, and to diagnose dianeutral transformations across them. Unfortunately, however, the locally referenced (*in-situ*) seawater density can vary substantially under purely adiabatic displacements (i.e. $\delta\Theta = \delta\mathrm{S} = 0$ but $\delta p \neq 0$), making it an inappropriate choice for a dynamically-useful density coordinate. These compressibility effects can be accounted for by instead considering the *potential density*,

$$\rho_r(\Theta, \mathrm{S}) \equiv \rho(\Theta, \mathrm{S}, r), \tag{43}$$

defined as the hypothetical density sea water would have if brought adiabatically to a constant reference pressure, $p = r$. Following Groeskamp et al. (2019), changes in potential density, ρ_r, can then be usefully expressed just in terms of changes in Conservative Temperature, Θ, and Absolute Salinity, S,

$$\delta\rho_r = \rho\left[-\left(-\frac{1}{\rho}\frac{\partial\rho_r}{\partial\Theta}\right)\delta\Theta + \left(\frac{1}{\rho}\frac{\partial\rho_r}{\partial \mathrm{S}}\right)\delta\mathrm{S}\right], \tag{44}$$

where $\alpha_r \equiv -\frac{1}{\rho}\frac{\partial\rho_r}{\partial\Theta}$ and $\beta_r \equiv \frac{1}{\rho}\frac{\partial\rho_r}{\partial \mathrm{S}}$ are both referenced to $p = r$. Dia-ρ_r transformations are thus simply diagnosed as

$$\frac{\mathrm{D}\rho_r}{\mathrm{D}t} = \rho\left(-\alpha_r\frac{\mathrm{D}\Theta}{\mathrm{D}t} + \beta_r\frac{\mathrm{DS}}{\mathrm{D}t}\right), \tag{45}$$

where $\alpha_r = \alpha_r(\boldsymbol{x}, t; r)$ is the (usually positive) thermal expansion coefficient, $\beta_r = \beta_r(\boldsymbol{x}, t; r) > 0$ is the positive haline contraction coefficient, and $\frac{\mathrm{D}}{\mathrm{D}t} \equiv \lim_{\delta t\to 0}\frac{\delta}{\delta t}$ is the material derivative. The density-coordinate calculations presented here take $r = 2000\,\mathrm{dbar}$ because budget diagnostics remapped online to the corresponding potential density ρ_2 were readily available.

While the global self-consistency of potential density surfaces is a useful characteristic for water mass analysis, it nevertheless suffers from two important interpretative limitations: 1) it is *in-situ* density, not potential density, that appears in the momentum equation and 2) away from the reference pressure, adiabatic displacements along potential density surfaces generally cause buoyant restoring forces, and thus dia-neutral transformation! In a potential density framework, we are therefore unable to isolate the desired dianeutral contributions to dia-ρ_r transformations from potentially non-negligible isoneutral contributions. This limitation is likely exacerbated for studies of deep ocean overturning, for which we would like to compare surface-forced water mass transformations (at $p = p_{\mathrm{atm}}$) against abyssal mixing-driven transformations (at $p > 4000\,\mathrm{dbar}$).

For global-scale water mass analysis, it would thus be desirable to define a *neutral density* variable that satisfies the following three desirable properties: 1) its isosurfaces are neutral surfaces, 2) it is quasi-material, i.e., changes only due to material transformations of temperature and salinity, and 3) is pycnotropic, i.e., can be expressed as a function of only *in-situ* density and pressure. While it turns out to be impossible to define exactly neutral surfaces for the global ocean, Stanley et al. (2021) demonstrate that it is possible to construct *approximately neutral surfaces* that satisfy property 1, and hence also properties 2 and 3, to a reasonable degree–or at least better than existing alternatives, such as the commonly-used “neutral density” variable proposed by Jackett and McDougall (1997) and later applied to WMT analysis by Iudicone et al. (2008). Future work includes extending our water mass transformation methods to density variables that are more neutral than potential density referenced to 2000 dbar, ρ_2.

In describing the conventional methods of water mass transformation analysis in detail, we have omitted a broader discussion of recent developments in water mass analysis that provide complementary perspectives: circulation and transformation in tracer-tracer coordinates (Zika et al., 2012; ?, ?; Evans et al., 2018), constant-mass partitioning (Sohail et al., 2023), Lagrangian water mass transformations (Döös et al., 2008; Tamsitt et al., 2018), internal tracer content (Holmes et al., 2019; Bladwell et al., 2021), water mass-based inverse methods (Zika & Taimoor, 2023), and applications to biogeochemistry (Iudicone et al., 2011). Practitioners of water mass analysis should choose whichever method (or combination of methods) best suits the problem at hand.

Budget diagnostics suitable for full WMT budget analysis are typically not available from commonly used repositories of ocean and climate model data, such as the CMIP ESGF data portals. For temperature, salinity, and density, surface water mass transformations and lateral convergent transports can be computed using monthly-mean surface flux and horizontal mass transport diagnostics, respectively, both of which are designated as Priority 1 in the OMIP protocol (Griffies et al., 2016). Full mass and tracer budget diagnostics, which include the interior mixing tendencies, are only asked to be saved at annual-mean resolution at Priority 3. The FAFMIP protocol elevates these annual-means to Priority 1 and asks for monthly-means at Priority 2; the monthly-mean diagnostics are useful for resolving the seasonal cycle of these budgets in geographical-depth space, but can result in substantial errors when transformed offline into tracer coordinates (compare rows of Figure 12). To our knowledge, snapshots of layer-thickness and tracer concentration/content, which are required at the bounds of the budget time-averaging intervals to accurately close the WMT budget, are not included in the OMIP, FAFMIP, or any other MIP protocol; however, it may be possible to approximate these tendencies sufficiently well for some use cases by finite-differencing monthly-mean layer thickness diagnostics and interpolating the results to the middle of the months. As demonstrated here, accurate WMT budgets require closed mass and tracer budgets that are either output at sufficiently high frequency–more often than monthly for global climate simulations–or are regridded and remapped online into the target tracer coordinate (see Figure 10). In either case, the raw data can be prohibitively large due to their four-dimensional nature and the large number of variables required to close the WMT budgets, which is presumably one reason these diagnostics are not already more available. At GFDL, this data proliferation problem has been mitigated in the development and production of mesoscale eddy-rich simulations by remapping to target tracer coordinates online and conservatively coarsening the diagnostics in time (as monthly- or annual-means) and in the horizontal dimensions (by integrating over 2x2 grid cell tiles). We argue that intercomparison of modeled WMT budgets would be sufficiently helpful for model development, evaluation, and analysis to warrant the inclusion of suitable ocean model diagnostics in future MIP protocols. We call on the community to initiate proof-of-concept inter-model comparisons in support of a Water Mass Model Intercomparison Project (WMMIP).

Provided that model data suitable for full WMT budgets becomes available, robust model intercomparison will require the standardization of analysis methods. As we have demonstrated here, there are several subtleties involved in the diagnosis of WMT budgets through which differences in implementation could introduce spurious inter-model differences. We developed the `xwmb` stack of Python packages (see Appendix D) as a model-agnostic community tool to standardize the diagnosis of WMT budgets in models and to facilitate robust model intercomparisons. For each distinct ocean model, the package only requires the specification of the model's grid geometry (using `xgcm`) and the structure of its mass and tracer budgets (using `xbudget`). Future work will extend support to arbitrary grid topologies such as the cubed-sphere grid of ECCOv4 (Forget et al., 2015) or the unstructured mesh of MPAS-Ocean (Ringler et al., 2013).

In conclusion, the development of increasingly comprehensive and high-resolution numerical ocean models requires new diagnostics that can extract meaning from the chaos; water mass transformation theory provides a framework for integrating these big and complex data sets to produce physically interpretable scalar budgets. The advances outlined here provide a set of best practices and software tools for robust calculations and interpretations of water mass transformation budgets–we encourage you to use them!

Appendix A Diagnosis of water mass transformation rates

A1 Relationship between advective- and flux-forms of the material derivative

Budget diagnostics for finite-volume ocean models are often not immediately available in the *intensive* form (16), $\rho \frac{\mathrm{D}\lambda}{\mathrm{D}t} = \rho \dot{\lambda}$, or

$$\rho \frac{\mathrm{D}\lambda}{\mathrm{D}t} \equiv \rho \left(\frac{\partial \lambda}{\partial t} + \boldsymbol{v} \cdot \boldsymbol{\nabla} \lambda \right) = -\boldsymbol{\nabla} \cdot \boldsymbol{J}, \tag{A1}$$

which exposes the advective-form material derivative that is necessary for the WMT budget approach outlined in Section 2. To write equation (A1), we have assumed all of the material transformation processes represented in $\rho\,\dot{\lambda}$ can be expressed as the convergence of a density-weighted tracer flux[1] $\boldsymbol{J}$, which we take to include fluxes across the ocean boundary (or, equivalently, the oceanic fluxes they induce infinitesimally close by).

Many ocean models employ discretizations that fall under the class of Generalized Vertical Coordinate (GVC) models (Chassignet et al., 2006), in which the GVC, denoted σ, is discretized in a number N of k-indexed layers of thickness $h_k \equiv \int_{\sigma_{k-1/2}}^{\sigma_{k+1/2}} z_\sigma \mathrm{d}\sigma$. The function $z(\sigma)$ must be a strictly monotonic mapping such that the specific thickness $z_\sigma \equiv \frac{\partial z}{\partial \sigma}$ (in σ-coordinates) is single-signed. In such models, tracer budgets are diagnosed in the *extensive* (layer-integrated) form (Griffies et al. (2020), eq. 32)

$$\frac{\partial(h_k\overline{\rho\lambda}^k)}{\partial t} + \boldsymbol{\nabla}_\sigma \cdot (h_k\overline{\rho\lambda\boldsymbol{u}}^k + h_k\overline{\boldsymbol{J}}^k) + \Delta_\sigma^k(\rho\lambda w^{(\dot{\sigma})} + J^{(\sigma)}) = 0 \tag{A2}$$

which also corresponds with the models' prognostic conservation equations. In equation (A2), overbars ($\overline{\phi}^k = \frac{1}{h_k}\int_{\sigma_{k-1/2}}^{\sigma_{k+1/2}} \phi\, z_\sigma \mathrm{d}\sigma$) denote the layer-average operation; $J^{(\sigma)} = z_\sigma \boldsymbol{\nabla}\sigma\cdot\boldsymbol{J}$ is the thickness-weighted dia-σ flux; $\boldsymbol{\nabla}_\sigma$ is the along-σ gradient; $\Delta_\sigma^k\phi = \phi(\sigma_{k+1/2}) - \phi(\sigma_{k-1/2})$ is the finite difference across the k^{th} layer; and ρ, λ, and $\boldsymbol{u}$ are the density, tracer concentration, and horizontal velocity, respectively. The dia-σ velocity component for the GVC is denoted by $w^{(\dot{\sigma})} \equiv z_\sigma \frac{\mathrm{D}\sigma}{\mathrm{D}t} \equiv z_\sigma\dot{\sigma}$, which is a normalization of the dia-σ advective mass flux in terms of a horizontal area element $\mathrm{d}A$, defined by $\rho\, w^{(\dot{\sigma})}\mathrm{d}A \equiv \rho\,(\boldsymbol{v} - \boldsymbol{v}^{(\sigma)}) \cdot \hat{\boldsymbol{n}}\mathrm{d}S$ (Griffies et al. (2020), Appendix D).

To recover the evolution equation (A1) for the intensive tracer concentration λ, we must remove from the extensive layer-integrated budget (A2) the effects of an evolving layer mass per unit area $\overline{h}\rho$, given by (Griffies et al. (2020), eq. 32b)

$$\frac{\partial(h_k\overline{\rho}^k)}{\partial t} + \boldsymbol{\nabla}_\sigma \cdot (h_k\overline{\rho\boldsymbol{v}}^k) + \Delta_\sigma^k(\rho\lambda w^{(\dot{\sigma})}) = 0. \tag{A3}$$

Since information has already been irreversibly lost by integration between the continuous form (A1) and the vertically discrete layer-integrated form (A2), however, we take a step back and consider the continuous versions of the thickness-weighted budgets (Griffies (2024), 58.4):

$$\frac{\partial(\rho z_\sigma\lambda)}{\partial t} + \boldsymbol{\nabla}_\sigma \cdot (\rho z_\sigma\lambda\boldsymbol{v}) + \frac{\partial}{\partial\sigma}(\rho z_\sigma\lambda\dot{\sigma}) = -\left[\boldsymbol{\nabla}_\sigma \cdot (z_\sigma\boldsymbol{J}) + \frac{\partial}{\partial\sigma}(z_\sigma\boldsymbol{\nabla}\sigma\cdot\boldsymbol{J})\right], \tag{A4}$$

$$\frac{\partial(\rho z_\sigma)}{\partial t} + \boldsymbol{\nabla}_\sigma \cdot (\rho z_\sigma\boldsymbol{v}) + \frac{\partial}{\partial\sigma}(\rho z_\sigma\dot{\sigma}) = 0. \tag{A5}$$

Note that under the Boussinesq approximation ($\boldsymbol{\nabla}\cdot\boldsymbol{v} = 0$) and with geopotential coordinates ($\sigma = z$), the specific cell thickness $z_\sigma = 1$ and reference density $\rho = \rho_0$ are constant and can be pulled out of the derivatives such that (A4) reduces trivially to (A1).

In the non-Boussinesq GVC case, expanding each of the LHS terms of (A4) using the product rule, we can write the respective terms in equation (A1) as:

$$\rho\frac{\partial\lambda}{\partial t} = \frac{1}{z_\sigma}\left[\frac{\partial(\rho z_\sigma\lambda)}{\partial t} - \lambda\frac{\partial(\rho z_\sigma)}{\partial t}\right] \tag{A6}$$

$$\rho\boldsymbol{v}\cdot\boldsymbol{\nabla}\lambda \equiv \rho\left(\boldsymbol{v}\cdot\boldsymbol{\nabla}_\sigma\lambda + \dot{\sigma}\frac{\partial\lambda}{\partial\sigma}\right) = \frac{1}{z_\sigma}\left[\boldsymbol{\nabla}_\sigma\cdot(\rho z_\sigma\lambda\boldsymbol{v}) - \lambda\boldsymbol{\nabla}_\sigma\cdot(\rho z_\sigma\boldsymbol{v}) + \frac{\partial}{\partial\sigma}(\rho z_\sigma\lambda\dot{\sigma}) - \lambda\frac{\partial}{\partial\sigma}(\rho z_\sigma\dot{\sigma})\right] \tag{A7}$$

$$\rho\dot{\lambda} = \frac{-1}{z_\sigma}\left[\boldsymbol{\nabla}_\sigma\cdot(z_\sigma\boldsymbol{J}) + \frac{\partial}{\partial\sigma}(z_\sigma\boldsymbol{\nabla}\sigma\cdot\boldsymbol{J})\right], \tag{A8}$$

[1] It is straight-forward to extend the method to include non-flux-form tracer sources and sinks; we leave these out to simplify the exposition as much as possible.

where each of the terms now corresponds directly with the continuous versions of the extensive tracer and mass budget diagnostics. To further connect these to finite-volume diagnostics, we now integrate (A6-A8) over discrete σ-layers, but first multiplying both sides by z_σ because the intensive λ-budgets only appear as thickness-weighted integrands, e.g. $\rho\frac{\partial\lambda}{\partial t}\mathrm{dV}$, where $\mathrm{d}V = \mathrm{d}z\mathrm{d}A = z_\sigma \mathrm{d}\sigma\mathrm{d}A$.

For the tendency term, the σ-integral commutes with time derivatives and we have

$$h_k\overline{\rho\frac{\partial\lambda}{\partial t}}^k \equiv \int_{\sigma_{k-1/2}}^{\sigma_{k+1/2}} \rho z_\sigma \frac{\partial\lambda}{\partial t}\mathrm{d}\sigma = \left[\frac{\partial}{\partial t}\right]_\sigma (h_k\overline{\rho\lambda}^k) - \int_{\sigma_{k-1/2}}^{\sigma_{k+1/2}} \lambda\frac{\partial(\rho z_\sigma)}{\partial t}\mathrm{d}\sigma = \left[\frac{\partial}{\partial t}\right]_\sigma (h_k\overline{\rho\lambda})^k - \overline{\lambda}_k\left[\frac{\partial}{\partial t}\right]_\sigma (h_k\overline{\rho}^k), \tag{A9}$$

where we have ignored intra-layer spatial correlations between λ and $\frac{\partial(\rho z_\sigma)}{\partial t}$.

For the advection term, derivatives also commute and we similarly arrive at

$$h_k\overline{\rho\boldsymbol{v}\cdot\boldsymbol{\nabla}\lambda}^k = \boldsymbol{\nabla}_\sigma\cdot(h_k\overline{\rho\lambda\boldsymbol{v}}^k) + \Delta^k_\sigma(\rho w^{(\dot{\sigma})}\lambda) - \overline{\lambda}^k\left[\boldsymbol{\nabla}_\sigma\cdot(h_k\overline{\rho\boldsymbol{v}}^k) + \Delta^k_\sigma(\rho w^{(\dot{\sigma})})\right]. \tag{A10}$$

For the non-conservative processes, we have

$$h_k\overline{\rho\dot{\lambda}}^k = -\left[\boldsymbol{\nabla}_\sigma\cdot(h_k\overline{\boldsymbol{J}}^k) + \Delta^k_\sigma J^{(\sigma)}\right]. \tag{A11}$$

Altogether, we have the following finite-volume expressions for the layer-mass-weighted λ-conservation equation

$$\left[\frac{\partial}{\partial t}\left(h_k\overline{\rho\lambda}^k\right) - \overline{\lambda}^k\frac{\partial}{\partial t}\left(\overline{\rho}^k h_k\right)\right] \qquad\qquad h_k\overline{\rho\frac{\partial\lambda}{\partial t}}^k \tag{A12}$$

$$+\left[\boldsymbol{\nabla}_\sigma\cdot(h_k\overline{\rho\lambda\boldsymbol{v}}^k) + \Delta^k_\sigma(\rho w^{(\dot{\sigma})}\lambda) - \overline{\lambda}^k\left(\boldsymbol{\nabla}_\sigma\cdot(h\overline{\rho\boldsymbol{v}}^k) + \Delta^k_\sigma(\rho w^{(\dot{\sigma})})\right)\right] \quad\Leftrightarrow\quad + h_k\overline{\rho\boldsymbol{v}\cdot\boldsymbol{\nabla}\lambda}^k \tag{A13}$$

$$= -\left[\boldsymbol{\nabla}_\sigma\cdot(h_k\overline{\boldsymbol{J}}^k) + \Delta^k_\sigma J^{(\sigma)}\right] \qquad\qquad = h_k\overline{\rho\dot{\lambda}}^k \tag{A14}$$

A2 Kinematics of normal-flux boundary conditions

We now turn to a discussion of the subtleties related to the treatment of kinematic boundary conditions on fluxes of seawater mass and tracer content. We will consider both advective exchange fluxes that reflect the exchange of mass between the ocean and other Earth system components (e.g. precipitation, evaporation, sea ice melt), as well as non-advective tracer exchange fluxes (e.g. turbulent air-sea fluxes, radiative heating/cooling, sea ice brine rejection).

We label the $N{+}1$ layer interfaces with integers ($k = 0, 1, ..., N$) and the N layer centers or layer averages with the half-steps between them ($k = \frac{1}{2}, ..., N{-}\frac{1}{2}$). This index notation is shifted by $\frac{1}{2}$ relative to that used by others (e.g. Griffies et al. (2020)); however, it greatly simplifies the interpretation of the following derivation. We take $k = 0$ to be the sea surface and $k = N$ the sea floor. Then, to explicitly reveal the influence of boundary conditions, we consider the three flux categories (bottom-interfacing, interior, surface-interfacing) separately[2]:

$$\begin{aligned}
&\text{(density-weighted tracer)} && \text{(mass)} && \text{(A15)}\\
&\Delta_\sigma^k(\rho w^{(\dot{\sigma})}\lambda + J^{(\sigma)}) && \Delta_\sigma^k(\rho w^{(\dot{\sigma})}) && \text{(A16)}\\
=&\Delta_\sigma^k\left(\mathcal{H}(k-N)\left[\rho w^{(\dot{\sigma})}\lambda + J^{(\sigma)}\right]\right) &= \;& \Delta_\sigma^k\left(\mathcal{H}(k-N)\left[\rho w^{(\dot{\sigma})}\right]\right) && \text{(bottom ocean fluxes)} \quad \text{(A17)}\\
+&\Delta_\sigma^k\left(\mathcal{I}_0^N(k)\left[\rho w^{(\dot{\sigma})}\lambda + J^{(\sigma)}\right]\right) &+ \;& \Delta_\sigma^k\left(\mathcal{I}_0^N(k)\left[\rho w^{(\dot{\sigma})}\right]\right) && \text{(interior ocean fluxes)} \quad \text{(A18)}\\
+&\Delta_\sigma^k\left(\mathcal{H}(-k)\left[\rho w^{(\dot{\sigma})}\lambda + J^{(\sigma)}\right]\right), &+ \;& \Delta_\sigma^k\left(\mathcal{H}(-k)\left[\rho w^{(\dot{\sigma})}\right]\right) && \text{, (surface ocean fluxes)} \quad \text{(A19)}
\end{aligned}$$

where $\mathcal{H}(n)$ is the Heaviside function (1 if $n \geq 0$; 0 otherwise) and $\mathcal{I}_i^j(k)$ is the interior function[3] (1 if $0 < k < N$; 0 otherwise). To illustrate the utility of the Heaviside function notation, consider the expressions for the ocean bottom fluxes (A17), which only have a nonzero contribution within the bottom-interfacing layer ($k = N-1/2$), where $\Delta_\sigma^k(\mathcal{H}(k-N)\phi) = \mathcal{H}(0)[\phi]_{k=N} - \mathcal{H}(-1)[\phi]_{k=N-1} = [\phi]_{k=N}$ is just the dia-seafloor flux, as desired. Since interior fluxes are typically already diagnosed in the form of expression (A18), where $\mathcal{I}_0^N(k)J^{(\sigma)}$ represent interior diffusive fluxes, we do not need to manipulate them any further. The surface and bottom oceanic fluxes, on the other hand, are provided only in terms of the interfacial advective and non-advective exchange fluxes that induce them.

At the bottom, the advective mass and tracer fluxes both vanish due to the no-normal flow boundary condition on the barycentric velocity ($\boldsymbol{v} \cdot \hat{\boldsymbol{n}} = 0$) at the static boundary ($\boldsymbol{v}^{(b)} = 0$), which together yield $\rho(\boldsymbol{v} - \boldsymbol{v}^{(b)}) \cdot \hat{\boldsymbol{n}}\mathrm{d}S = 0$ and thus $\rho w^{(\dot{\sigma})} = 0$. However, there may still be a nonzero non-advective tracer transport (e.g. geothermal heat flux), which we denote as $J^{(\sigma)} \equiv -Q_\lambda^{\text{bot}}$ such that $Q_\lambda^{\text{bot}} > 0$ indicates an input of density-weighted λ to the ocean. Thus, we write the bottom fluxes as

$$\left[J^{(\sigma)}\right]_{k=N} = -Q_\lambda^{\text{bot}} \tag{A20}$$
$$\left[\rho w^{(\dot{\sigma})}\right]_{k=N} = 0 \tag{A21}$$

At the sea surface, the mass flux Q_M^{surf} (e.g. due to precipitation, evaporation, sea ice melt) is, by definition, purely advective, yielding the straight-forward equivalence

$$\left[\rho w^{(\dot{\sigma})}\right]_{k=0} = -Q_M^{\text{surf}}. \tag{A22}$$

By contrast, the net density-weighted tracer exchange flux Q_λ^{net} must be treated carefully because it includes a non-advective component as well as an advective component associated with the tracer content of the water being exchanged,

$$Q_\lambda^{\text{net}} = \lambda_M Q_M^{\text{surf}} + Q_\lambda^{\text{surf}}, \tag{A23}$$

[2] In practice, this conceptual approach is complicated by the fact that some boundary fluxes (most notably incoming solar radiation) penetrate across the interfaces and into the interior ocean, resulting in a non-negligible interior flux-divergence (Iudicone et al., 2008). It is nevertheless useful to distinguish the boundary-related processes from interior processes such as diffusion.

[3] The interior function differs from conventional boxcar functions because it excludes the endpoints.

where λ_M is the tracer concentration of the exchanged water mass[4]. Within an infinitesimal skin layer of the surface ocean, this boundary exchange flux induces both an advective oceanic flux and a non-advective oceanic flux:

$$Q_\lambda^{\text{net}} = -\left[\rho w^{\dot\sigma}\lambda + J^{(\sigma)}\right]_{k=0} = [\lambda]_{k=0}\, Q_M^{\text{surf}} - \left[J^{(\sigma)}\right]_{k=0}. \tag{A24}$$

Equating the RHS expressions of (A23) and (A24) yields an expression for the induced non-advective oceanic flux in terms of the non-advective tracer exchange flux and the advective mass flux:

$$[J^\sigma]_{k=0} = -Q_\lambda^{\text{surf}} - (\lambda_M - [\lambda]_{k=0})Q_M^{\text{surf}}. \tag{A25}$$

In summary, plugging the above expressions back into equation (A19), we have

$$\left[J^{(\sigma)}\right]_{k=0} = -Q_\lambda^{\text{surf}} - (\lambda_M - [\lambda]_{k=0})Q_M^{\text{surf}} \tag{A26}$$

$$\left[\rho w^{(\dot\sigma)}\right]_{k=0} = -Q_M^{\text{surf}} \tag{A27}$$

$$\left[\rho w^{(\dot\sigma)}\lambda\right]_{k=0} = -[\lambda]_{k=0}\, Q_M^{\text{surf}} \tag{A28}$$

Altogether, plugging expressions (A20, A21, A26, A28, A27) into (A17–A19) we have

$$\left[\frac{\partial}{\partial t}\left(h_k\overline{\rho\lambda}^k\right) - \overline{\lambda}^k\frac{\partial}{\partial t}\left(\overline{\rho}^k h_k\right)\right] \tag{A29}$$

$$+\left[\boldsymbol{\nabla}_\sigma\cdot(h_k\overline{\rho\lambda\boldsymbol{v}}^k) + \Delta_\sigma^k\left(\mathcal{I}_0^N(k)\rho w^{(\dot\sigma)}\lambda - \mathcal{H}(-k)\lambda Q_M^{\text{surf}}\right)\right] \tag{A30}$$

$$-\overline{\lambda}^k\left[\left(\boldsymbol{\nabla}_\sigma\cdot(h\overline{\rho\boldsymbol{v}}^k) + \Delta_\sigma^k(\mathcal{I}_0^N(k)\rho w^{(\dot\sigma)} - \mathcal{H}(-k)Q_M^{\text{surf}}\right)\right] \tag{A31}$$

$$= -\left[\boldsymbol{\nabla}_\sigma\cdot(h_k\overline{\boldsymbol{J}}^k) + \Delta_\sigma^k\left(\mathcal{I}_0^N(k)J^{(\sigma)} - \mathcal{H}(-k)\left[Q_\lambda^{\text{surf}} + (\lambda_M-\lambda)Q_M^{\text{surf}}\right] - \mathcal{H}(k-N))Q_\lambda^{\text{bot}}\right)\right]. \tag{A32}$$

If the Eulerian time derivative and advective components of the material derivative do not need to be distinguished, then the terms with the common factor $\overline{\lambda}^k$ outside of the deriative/difference operators can be collectively identified as the conservative equation for layer-integrated mass (A3), which therefore vanishes. We are left with:

$$h_k\overline{\rho\left(\frac{\partial\lambda}{\partial t} + \boldsymbol{v}\cdot\boldsymbol{\nabla}\lambda\right)}^k \tag{A33}$$

$$= \left[\frac{\partial}{\partial t}\left(h_k\overline{\rho\lambda}^k\right) + \boldsymbol{\nabla}_\sigma\cdot(h_k\overline{\rho\lambda\boldsymbol{v}}^k) + \Delta_\sigma^k\left(\mathcal{I}_0^N(k)\rho w^{(\dot\sigma)}\lambda\right) - \Delta_\sigma^k\left(\mathcal{H}(-k)\lambda Q_M^{\text{surf}}\right)\right] \tag{A34}$$

$$= -\left[\boldsymbol{\nabla}_\sigma\cdot(h_k\overline{\boldsymbol{J}}^k) + \Delta_\sigma^k\left(\mathcal{I}_0^N(k)J^{(\sigma)} - \mathcal{H}(-k)\left[Q_\lambda^{\text{surf}} + (\lambda_M-\lambda)Q_M^{\text{surf}}\right] - \mathcal{H}(-(N-k))Q_\lambda^{\text{bot}}\right)\right]. \tag{A35}$$

Expression (A33) is the density-weighted and layer-integrated advective form of the kinematic material derivative; expression (A34) is the *flux form of the kinematic material deriative*; and expression (A35) is the *flux-form of the non-conservative process-based material derivative*. Breaking the budget down into the contributions from different classes

[4] This term could in principle be represented as the aggregate of multiple different mass fluxes, each carrying different mean tracer concentrations. In practice, assumptions are often much simpler; in MOM6, for example, both the in- and out-flowing water masses are assumed to have the same Conservative Temperature as the surface layer ($\Theta_M = \overline{\Theta}^{k=0}$) and to be pure freshwater ($S_M = 0$).

of physical processes, we assign the following labels:

$$\frac{\partial}{\partial t}\left(h_k\overline{\rho\lambda}^k\right) \qquad \text{(Eulerian layer tendency)} \tag{A36}$$
$$+\boldsymbol{\nabla}_\sigma \cdot (h_k\overline{\rho\lambda\boldsymbol{v}}^k) \qquad \text{(Along-surface lateral advection)} \tag{A37}$$
$$+\Delta_\sigma^k\left(\mathcal{I}_0^N(k)\rho w^{(\dot{\sigma})}\lambda\right) \qquad \text{(Dia-interface advection, i.e. regridding/remapping)} \tag{A38}$$
$$-\Delta_\sigma^k\left(\mathcal{H}(-k)\lambda Q_M^{\text{surf}}\right) = \qquad \text{(Advective ocean tracer flux at surface)} \tag{A39}$$
$$-\boldsymbol{\nabla}_\sigma \cdot (h_k\overline{\boldsymbol{J}}^k) \qquad \text{(Along-layer lateral diffusion)} \tag{A40}$$
$$-\Delta_\sigma^k\left(\mathcal{I}_0^N(k)J^{(\sigma)}\right) \qquad \text{(Dia-interface turbulent diffusion)} \tag{A41}$$
$$+\Delta_\sigma^k\left(\mathcal{H}(-k)\left[Q_\lambda^{\text{surf}} + (\lambda_M - \lambda)Q_M^{\text{surf}}\right]\right) \qquad \text{(Non-advective ocean tracer flux at surface)} \tag{A42}$$
$$+\Delta_\sigma^k\left(\mathcal{H}(-(N-k))Q_\lambda^{\text{bot}}\right). \qquad \text{(Non-advective ocean tracer flux at bottom)} \tag{A43}$$

This partitioning of the layer-integrated tracer budget is useful because it is consistent with the kinematic–process partitioning of the λ-WMT equation (24), allowing the integrals appearing therein to be approximated by Riemann sums and computed by 1) appropriately area-weighting the terms (A36-A43), 2) vertically-remapping them to λ-coordinates, 3) and summing them over the discrete water class $\Delta\Omega(\tilde{\lambda}, t) \equiv \Omega(\lambda + \Delta\lambda/2, t)\backslash\Omega(\lambda - \Delta\lambda/2, t)$, where $\backslash$ denotes the set difference, as described in Section 3.

Appendix B Water mass transformation rates from MOM6 diagnostics

The terms identified in expressions (A36-A43) are nearly identical to those available as layer-integrated tracer-budget diagnostics in MOM6,

$$\frac{\partial}{\partial t}\left(h_k\overline{\rho\lambda}^k\right) = \qquad \text{(Eulerian layer tendency)} \tag{B1}$$
$$-\boldsymbol{\nabla}_\sigma \cdot (h_k\overline{\rho\lambda\boldsymbol{v}}^k) \qquad \text{(Along-layer advection)} \tag{B2}$$
$$-\Delta_\sigma^k\left(\mathcal{I}_0^N(k)\rho w^{(\dot{\sigma})}\lambda\right) \qquad \text{(Dia-interface advection, i.e. regridding/remapping)} \tag{B3}$$
$$-\boldsymbol{\nabla}_\sigma \cdot (h_k\overline{\boldsymbol{J}}^k) \qquad \text{(Along-surface lateral diffusion)} \tag{B4}$$
$$-\Delta_\sigma^k\left(\mathcal{I}_0^N(k)J^{(\sigma)}\right) \qquad \text{(Dia-interface turbulent diffusion)} \tag{B5}$$
$$+\Delta_\sigma^k\left(\mathcal{H}(-k)\left[Q_\lambda^{\text{surf}} + \lambda_M Q_M^{\text{surf}}\right]\right) \qquad \text{(Surface tracer flux)} \tag{B6}$$
$$+\Delta_\sigma^k\left(\mathcal{H}(-(N-k))Q_\lambda^{\text{bot}}\right). \qquad \text{(Non-advective bottom tracer flux),} \tag{B7}$$

Terms B2 and B3 can be moved to the LHS by changing signs. The more problematic discrepancy is that, in the presently available layer-integrated MOM6 diagnostics, all of the surface ocean tracer flux terms are bundled together (expression B6) and thus are not readily decomposed into their purely advective part (A39), which contributes to the kinematic material derivative (LHS), and the non-advective part (A42), which contributes to the process-based material derivative (RHS). This means that the layer-integrated budget diagnostics, as currently implemented, are inconsistent with the water mass transformation approach! In the Baltic sea test case presented here, the erroneous transformations due to the omitted advective ocean tracer flux divergence term $\Delta_\sigma^k\left(\mathcal{H}(-k)\lambda Q_M^{\text{surf}}\right)$ are, relative to other terms in the budget, $\mathcal{O}(10^{-2})$ for temperature but $\mathcal{O}(1)$ for salinity (for which $\lambda_M = 0$ by assumption for freshwater, whereas $\lambda = \mathcal{O}(30)$ ppt) and therefore can not be neglected.

While neither the advective ocean tracer flux divergence $\Delta_\sigma^k\left(\mathcal{H}(-k)\lambda Q_M^{\text{surf}}\right)$ nor the non-advective ocean tracer flux divergence $\Delta_\sigma^k\left(\mathcal{H}(-k)\left[Q_\lambda^{\text{surf}} + (\lambda_M - \lambda)Q_M^{\text{surf}}\right]\right)$ are directly available as layer-integrated budget tendencies, they can be nevertheless be estimated offline from the product of $[\lambda]^{k=0}$ (often set to the upper-most layer's concentration $[\lambda]^{k=\frac{1}{2}}$) and Q_M^{surf}. However, this offline operation inevitably omits temporal correlation terms below the diagnostic averaging period, thereby introducing errors into the otherwise exact budget. We recommend this approach eventually be replaced by a new online diagnostic for $\lambda Q_M^{\text{surf}}$, ideally as a three-dimensional layer-integrated budget tendency. In any case, subtracting the advective ocean tracer flux term from both sides of equation (B1-B7) and rearranging the layer-integrated budget into the kinematic part (LHS) and non-conservative process-based part (RHS), we arrive at the desired equation (A36-A43).

Appendix C Boussinesq relationships

Under the Boussinesq approximation, the flow field is non-divergent ($\boldsymbol{\nabla}\cdot\boldsymbol{v} = 0$), which one might expect to simplify the water mass (or volume) budget. For instance, directly integrating the continuity equation $\boldsymbol{\nabla}\cdot\boldsymbol{v} = 0$ over $\Omega(\tilde{\lambda}, t)$ and following a similar logic as in the above section, we have

$$-\int_\Omega \boldsymbol{\nabla}\cdot\boldsymbol{v}\mathrm{d}V = -\oint_{\partial\Omega} \boldsymbol{v}\cdot\hat{\boldsymbol{n}}^{(\partial\Omega)}\mathrm{d}S = -\int_{\partial\Omega_{\text{surf}}} \boldsymbol{v}\cdot\hat{\boldsymbol{n}}^{(s)}\mathrm{d}S - \int_{\partial\mathcal{R}} \boldsymbol{u}\cdot\hat{\boldsymbol{n}}^{(\partial\mathcal{R})}\mathrm{d}S - \partial\lambda\int_\Omega \boldsymbol{v}\cdot\boldsymbol{\nabla}\lambda\mathrm{d}V = 0. \tag{C1}$$

Additionally, by applying Leibniz' integral rule (6) to the volume budget (i.e., setting $F = 1$ instead of $F = \rho$), we have

$$\partial_t\mathcal{V}_\Omega \equiv \partial_t\int_\Omega \mathrm{d}V = \oint_{\partial\Omega} \boldsymbol{v}^{(\partial\Omega)}\cdot\hat{\boldsymbol{n}}\mathrm{d}S = \int_{\partial\Omega_{\text{surf}}} \boldsymbol{v}^{(s)}\cdot\hat{\boldsymbol{n}}^{(s)}\mathrm{d}S - \partial_{\tilde{\lambda}}\int_\Omega \frac{\partial\lambda}{\partial t}\mathrm{d}V. \tag{C2}$$

Summing (C1) and (C2), and using equation (16), yields a λ-water volume budget

$$\partial_t\mathcal{V}_\Omega + \int_{\partial\Omega_{\text{surf}}} (\boldsymbol{v} - \boldsymbol{v}^{(s)})\cdot\hat{\boldsymbol{n}}^{(s)}\mathrm{d}S + \int_{\partial\mathcal{R}} \boldsymbol{u}\cdot\hat{\boldsymbol{n}}^{(\partial\mathcal{R})}\mathrm{d}S = -\partial_{\tilde{\lambda}}\left[\int_\Omega \dot{\lambda}\,\mathrm{d}V\right], \tag{C3}$$

which is, modulo a reference density $\rho = \rho_0$, identical to the λ-WMT budget (29).

In theory, the possibility of separately evaluating the two components (C1 and C2) might provide more granular insight into the WMT budget. Because boundary mass fluxes Q_M^{surf} are implemented directly in terms of the relative velocity $\boldsymbol{v}-\boldsymbol{v}^{(s)}$, equations (C1) and (C2) are intrinsically coupled and can not be separately evaluated. In many cases, however, the surface mass flux only plays a minor role in the water volume budget, such that the following approximate relationships can still be useful (see Bailey et al., 2023):

$$\partial_t\mathcal{V}_\Omega \simeq -\partial_{\tilde{\lambda}}\int_\Omega \frac{\partial\lambda}{\partial t}\mathrm{d}V \tag{C4}$$

$$\int_{\partial\mathcal{R}\,\cap\,\{\lambda\leq\tilde{\lambda}\}} \boldsymbol{u}\cdot\hat{\boldsymbol{n}}^{(\partial\mathcal{R})}\mathrm{d}S = -\partial_{\tilde{\lambda}}\int_\Omega \boldsymbol{v}\cdot\boldsymbol{\nabla}\lambda\mathrm{d}V \tag{C5}$$

The utility of these approximate relationships may carry over to the non-Boussinesq case, even as they become even less exact.

Appendix D Open Research

The calculations described above make use of a stack of new open-source Python packages, which leverage data structures and methods from `xarray` (Hoyer & Hamman,

2017) and `xgcm` (Abernathey et al., 2022) for out-of-memory operations on finite volume model grids.

[Proper archiving and referencing of the following packages will be deferred to a later stage of the publication process]. We use the new package `regionate` to define our discretized regions R on the model grid and an updated version of `sectionate` to accumulate mass transports normal to the boundary ∂R (see also Section 3.2). Water mass properties and transformation rates are evaluated using an updated version of `xwmt` (Tesdal et al., 2023). The remaining terms in the water mass budget are computed with the new package `xwmb`. An additional package, `xbudget`, provides helper functions for wrangling complicated multi-level tracer budget diagnostics and is used to verify budget closure and decompose high-level terms into constituent processes. All of the packages are designed to be agnostic to the specific formulation of the FV-GVC ocean model to promote community uptake and facilitate inter-model comparisons, requiring only that users provide metadata describing each model's grid geometry/topology and diagnostic mass/tracer budgets. The current implementations only support curvilinear grid but future work aims to develop support for arbitrary grid-face topologies (e.g. cubed-sphere) and grid geometries (i.e. unstructured triangular or hexagonal horizontal grids).

Acknowledgments

H.F.D. acknowledges support from the NOAA C&GC Fellowship (AWARD NO.) and UC Irvine's School of Physical Sciences.

References

Abernathey, R. P., Busecke, J. J. M., Smith, T. A., Deauna, J. D., Banihirwe, A., Nicholas, T., … Thielen, J. (2022, November). *xgcm.* Zenodo. Retrieved 2023-08-07, from https://zenodo.org/record/7348619 doi: 10.5281/zenodo.7348619

Adcroft, A., Anderson, W., Balaji, V., Blanton, C., Bushuk, M., Dufour, C. O., … Zhang, R. (2019). The GFDL Global Ocean and Sea Ice Model OM4.0: Model Description and Simulation Features. *Journal of Advances in Modeling Earth Systems*, *11*(10), 3167–3211. Retrieved 2020-12-06, from https://agupubs.onlinelibrary.wiley.com/doi/abs/10.1029/2019MS001726 (_eprint: https://agupubs.onlinelibrary.wiley.com/doi/pdf/10.1029/2019MS001726) doi: https://doi.org/10.1029/2019MS001726

Bailey, S. T., Jones, C. S., Abernathey, R. P., Gordon, A. L., & Yuan, X. (2023, April). Water mass transformation variability in the Weddell Sea in ocean reanalyses. *Ocean Science*, *19*(2), 381–402. Retrieved 2023-07-21, from https://os.copernicus.org/articles/19/381/2023/ (Publisher: Copernicus GmbH) doi: 10.5194/os-19-381-2023

Bladwell, C., Holmes, R. M., & Zika, J. D. (2021, July). Internal Salt Content: A Useful Framework for Understanding the Oceanic Branch of the Water Cycle. *Journal of Physical Oceanography*, *51*(7), 2167–2179. Retrieved 2024-02-27, from https://journals.ametsoc.org/view/journals/phoc/51/7/JPO-D-20-0212.1.xml (Publisher: American Meteorological Society Section: Journal of Physical Oceanography) doi: 10.1175/JPO-D-20-0212.1

Broecker, W. S. (1982). *Tracers in the Sea* (Edition unstated ed.). Eldigio Pr.

Burchard, H., & Rennau, H. (2008). Comparative quantification of physically and numerically induced mixing in ocean models. *Ocean Modelling*, *20*, 293–311.

Cessi, P. (2019). The Global Overturning Circulation. *Annual Review of Marine Science*, *11*(1), 249–270. Retrieved 2022-01-08, from https://doi.org/10.1146/annurev-marine-010318-095241 (_eprint: https://doi.org/10.1146/annurev-marine-010318-095241) doi: 10.1146/annurev-marine-010318-095241

Chassignet, E., Hurlburt, H., Smedstad, O. M., Halliwell, G., Wallcraft, A., Metzger,

E. J., ... Srinivasan, A. (2006, March). Generalized Vertical Coordinates for Eddy-Resolving Global and Coastal Ocean Forecasts. *Oceanography*, *19*(1), 118–129. Retrieved 2024-02-29, from https://tos.org/oceanography/article/generalized-vertical-coordinates-for-eddy-resolving-global-and-coastal-ocea doi: 10.5670/oceanog.2006.95

de Lavergne, C., Madec, G., Le Sommer, J., Nurser, A. J. G., & Naveira Garabato, A. C. (2016, February). On the Consumption of Antarctic Bottom Water in the Abyssal Ocean. *Journal of Physical Oceanography*, *46*(2), 635–661. Retrieved 2019-01-02, from http://journals.ametsoc.org/doi/10.1175/JPO-D-14-0201.1 doi: 10.1175/JPO-D-14-0201.1

Deppenmeier, A.-L., Bryan, F. O., Kessler, W. S., & Thompson, L. (2022, October). Diabatic Upwelling in the Tropical Pacific: Seasonal and Subseasonal Variability. *Journal of Physical Oceanography*, *52*(11), 2657–2668. Retrieved 2023-07-20, from https://journals.ametsoc.org/view/journals/phoc/52/11/JPO-D-21-0316.1.xml (Publisher: American Meteorological Society Section: Journal of Physical Oceanography) doi: 10.1175/JPO-D-21-0316.1

Döös, K., Nilsson, J., Nycander, J., Brodeau, L., & Ballarotta, M. (2012). The World Ocean thermohaline circulation. *Journal of Physical Oceanography*, *42*, 1445–1460. doi: 10.1175/JPO-D-11-0163.1

Drake, H. F., Ferrari, R., & Callies, J. (2020, August). Abyssal Circulation Driven by Near-Boundary Mixing: Water Mass Transformations and Interior Stratification. *Journal of Physical Oceanography*, *50*(8), 2203–2226. Retrieved 2020-11-29, from https://journals.ametsoc.org/jpo/article/50/8/2203/348530/Abyssal-Circulation-Driven-by-Near-Boundary-Mixing (Publisher: American Meteorological Society) doi: 10.1175/JPO-D-19-0313.1

Drake, H. F., Ruan, X., & Ferrari, R. (2022, November). Diapycnal Displacement, Diffusion, and Distortion of Tracers in the Ocean. *Journal of Physical Oceanography*, *52*(12), 3221–3240. Retrieved 2022-12-02, from https://journals.ametsoc.org/view/journals/phoc/52/12/JPO-D-22-0010.1.xml (Publisher: American Meteorological Society Section: Journal of Physical Oceanography) doi: 10.1175/JPO-D-22-0010.1

Döös, K., Nycander, J., & Coward, A. C. (2008). Lagrangian decomposition of the Deacon Cell. *Journal of Geophysical Research: Oceans*, *113*(7), 1–13. (ISBN: 0148-0227) doi: 10.1029/2007JC004351

Döös, K., & Webb, D. J. (1994, February). The Deacon Cell and the Other Meridional Cells of the Southern Ocean. *Journal of Physical Oceanography*, *24*(2), 429–442. Retrieved 2018-05-08, from http://journals.ametsoc.org/doi/abs/10.1175/1520-0485%281994%29024%3C0429%3ATDCATO%3E2.0.CO%3B2 doi: 10.1175/1520-0485(1994)024⟨0429:TDCATO⟩2.0.CO;2

Evans, D. G., Holliday, N. P., Bacon, S., & Le Bras, I. (2023, June). Mixing and air–sea buoyancy fluxes set the time-mean overturning circulation in the subpolar North Atlantic and Nordic Seas. *Ocean Science*, *19*(3), 745–768. Retrieved 2023-09-18, from https://os.copernicus.org/articles/19/745/2023/ (Publisher: Copernicus GmbH) doi: 10.5194/os-19-745-2023

Evans, D. G., Zika, J. D., Naveira Garabato, A. C., & Nurser, A. J. G. (2018). The Cold Transit of Southern Ocean Upwelling. *Geophysical Research Letters*, *45*(24), 13,386–13,395. Retrieved 2024-02-27, from https://onlinelibrary.wiley.com/doi/abs/10.1029/2018GL079986 (_eprint: https://onlinelibrary.wiley.com/doi/pdf/10.1029/2018GL079986) doi: 10.1029/2018GL079986

Ferrari, R., Mashayek, A., McDougall, T. J., Nikurashin, M., & Campin, J.-M. (2016, July). Turning Ocean Mixing Upside Down. *Journal of Physical Oceanography*, *46*(7), 2239–2261. Retrieved 2019-01-02, from http://journals.ametsoc.org/doi/10.1175/JPO-D-15-0244.1 doi: 10.1175/JPO-D-15-0244.1

Ferrari, R., & Wunsch, C. (2009). Ocean Circulation Kinetic Energy: Reservoirs, Sources, and Sinks. *Annual Review of Fluid Mechanics*, *41*(1), 253–282. (ISBN: 0066-4189) doi: 10.1146/annurev.fluid.40.111406.102139

Forget, G., Campin, J.-M., Heimbach, P., Hill, C. N., Ponte, R. M., & Wunsch, C. (2015, October). ECCO version 4: an integrated framework for non-linear inverse modeling and global ocean state estimation. *Geoscientific Model Development*, *8*(10), 3071–3104. Retrieved 2023-08-01, from https://gmd.copernicus.org/articles/8/3071/2015/ (Publisher: Copernicus GmbH) doi: 10.5194/gmd-8-3071-2015

Fox-Kemper, B., Adcroft, A., Böning, C. W., Chassignet, E. P., Curchitser, E., Danabasoglu, G., … Yeager, S. G. (2019). Challenges and Prospects in Ocean Circulation Models. *Frontiers in Marine Science*, *6*. Retrieved 2023-08-01, from https://www.frontiersin.org/articles/10.3389/fmars.2019.00065

Griffies, S. M. (2024). *Geophysical Fluid Mechanics.* (Draft available at https://stephengriffies.github.io/assets/pdfs/GFM_lectures.pdf)

Griffies, S. M., Adcroft, A., & Hallberg, R. W. (2020). A Primer on the Vertical Lagrangian-Remap Method in Ocean Models Based on Finite Volume Generalized Vertical Coordinates. *Journal of Advances in Modeling Earth Systems*, *12*(10), e2019MS001954. Retrieved 2023-10-11, from https://onlinelibrary.wiley.com/doi/abs/10.1029/2019MS001954 (_eprint: https://onlinelibrary.wiley.com/doi/pdf/10.1029/2019MS001954) doi: 10.1029/2019MS001954

Griffies, S. M., Danabasoglu, G., Durack, P. J., Adcroft, A. J., Balaji, V., Böning, C. W., … Yeager, S. G. (2016, September). OMIP contribution to CMIP6: experimental and diagnostic protocol for the physical component of the Ocean Model Intercomparison Project. *Geoscientific Model Development*, *9*(9), 3231–3296. Retrieved 2024-02-27, from https://gmd.copernicus.org/articles/9/3231/2016/ (Publisher: Copernicus GmbH) doi: 10.5194/gmd-9-3231-2016

Griffies, S. M., Pacanowski, R. C., & Hallberg, R. W. (2000, March). Spurious Diapycnal Mixing Associated with Advection in a z -Coordinate Ocean Model. *Monthly Weather Review*, *128*(3), 538–564. Retrieved 2018-10-20, from http://journals.ametsoc.org/doi/abs/10.1175/1520-0493%282000%29128%3C0538%3ASDMAWA%3E2.0.CO%3B2 doi: 10.1175/1520-0493(2000)128⟨0538:SDMAWA⟩2.0.CO;2

Groeskamp, S., Griffies, S. M., Iudicone, D., Marsh, R., Nurser, A. G., & Zika, J. D. (2019). The Water Mass Transformation Framework for Ocean Physics and Biogeochemistry. *Annual Review of Marine Science*, *11*(1), 271–305. Retrieved 2022-11-04, from https://doi.org/10.1146/annurev-marine-010318-095421 (_eprint: https://doi.org/10.1146/annurev-marine-010318-095421) doi: 10.1146/annurev-marine-010318-095421

Groeskamp, S., Zika, J. D., McDougall, T. J., Sloyan, B. M., & Laliberté, F. (2014, July). The Representation of Ocean Circulation and Variability in Thermodynamic Coordinates. *Journal of Physical Oceanography*, *44*(7), 1735–1750. Retrieved 2023-08-31, from https://journals.ametsoc.org/view/journals/phoc/44/7/jpo-d-13-0213.1.xml (Publisher: American Meteorological Society Section: Journal of Physical Oceanography) doi: 10.1175/JPO-D-13-0213.1

Held, I. M., Guo, H., Adcroft, A., Dunne, J. P., Horowitz, L. W., Krasting, J., … Zadeh, N. (2019). Structure and Performance of GFDL's CM4.0 Climate Model. *Journal of Advances in Modeling Earth Systems*, *11*(11), 3691–3727. Retrieved 2022-12-12, from https://onlinelibrary.wiley.com/doi/abs/10.1029/2019MS001829 (_eprint: https://onlinelibrary.wiley.com/doi/pdf/10.1029/2019MS001829) doi: 10.1029/2019MS001829

Hill, C., Ferreira, D., Campin, J.-M., Marshall, J., Abernathey, R., & Barrier, N.

(2012, January). Controlling spurious diapycnal mixing in eddy-resolving height-coordinate ocean models – Insights from virtual deliberate tracer release experiments. *Ocean Modelling*, *45-46*, 14–26. Retrieved 2023-08-28, from https://www.sciencedirect.com/science/article/pii/S1463500311001880 doi: 10.1016/j.ocemod.2011.12.001

Holmes, R. M., Zika, J. D., & England, M. H. (2019, January). Diathermal Heat Transport in a Global Ocean Model. *Journal of Physical Oceanography*, *49*(1), 141–161. Retrieved 2024-02-27, from https://journals.ametsoc.org/view/journals/phoc/49/1/jpo-d-18-0098.1.xml (Publisher: American Meteorological Society Section: Journal of Physical Oceanography) doi: 10.1175/JPO-D-18-0098.1

Holmes, R. M., Zika, J. D., Griffies, S. M., Hogg, A. M., Kiss, A. E., & England, M. H. (2021). The Geography of Numerical Mixing in a Suite of Global Ocean Models. *Journal of Advances in Modeling Earth Systems*, *13*(7), e2020MS002333. Retrieved 2023-08-01, from https://onlinelibrary.wiley.com/doi/abs/10.1029/2020MS002333 (_eprint: https://onlinelibrary.wiley.com/doi/pdf/10.1029/2020MS002333) doi: 10.1029/2020MS002333

Hoyer, S., & Hamman, J. (2017, April). xarray: N-D labeled Arrays and Datasets in Python. , *5*(1), 10. Retrieved 2023-08-07, from https://openresearchsoftware.metajnl.com/articles/10.5334/jors.148 (Number: 1 Publisher: Ubiquity Press) doi: 10.5334/jors.148

Huang, R. (2005, January). Available potential energy in the world's ocean. *Journal of Marine Research*, *63*. doi: 10.1357/0022240053693770

Ilıcak, M., Adcroft, A. J., Griffies, S. M., & Hallberg, R. W. (2012, January). Spurious dianeutral mixing and the role of momentum closure. *Ocean Modelling*, *45-46*, 37–58. Retrieved 2023-08-28, from https://www.sciencedirect.com/science/article/pii/S1463500311001685 doi: 10.1016/j.ocemod.2011.10.003

Iselin, C. O. (1939). The influence of vertical and lateral turbulence on the characteristics of the waters at mid-depth. *EOS*, *3*, 414–417.

Iudicone, D., Madec, G., & McDougall, T. J. (2008, July). Water-Mass Transformations in a Neutral Density Framework and the Key Role of Light Penetration. *Journal of Physical Oceanography*, *38*(7), 1357–1376. Retrieved 2023-08-28, from https://journals.ametsoc.org/view/journals/phoc/38/7/2007jpo3464.1.xml (Publisher: American Meteorological Society Section: Journal of Physical Oceanography) doi: 10.1175/2007JPO3464.1

Iudicone, D., Rodgers, K. B., Stendardo, I., Aumont, O., Madec, G., Bopp, L., … Ribera d'Alcala', M. (2011, May). Water masses as a unifying framework for understanding the Southern Ocean Carbon Cycle. *Biogeosciences*, *8*(5), 1031–1052. Retrieved 2024-02-27, from https://bg.copernicus.org/articles/8/1031/2011/ (Publisher: Copernicus GmbH) doi: 10.5194/bg-8-1031-2011

Jackett, D. R., & McDougall, T. J. (1997, February). A Neutral Density Variable for the World's Oceans. *Journal of Physical Oceanography*, *27*(2), 237–263. Retrieved 2019-01-02, from http://journals.ametsoc.org/doi/abs/10.1175/1520-0485%281997%29027%3C0237%3AANDVFT%3E2.0.CO%3B2 doi: 10.1175/1520-0485(1997)027⟨0237:ANDVFT⟩2.0.CO;2

Lee, M.-M., Coward, A. C., & Nurser, A. J. G. (2002, May). Spurious Diapycnal Mixing of the Deep Waters in an Eddy-Permitting Global Ocean Model. *Journal of Physical Oceanography*, *32*(5), 1522–1535. Retrieved 2023-08-01, from https://journals.ametsoc.org/view/journals/phoc/32/5/1520-0485_2002_032_1522_sdmotd_2.0.co_2.xml (Publisher: American Meteorological Society Section: Journal of Physical Oceanography) doi: 10.1175/1520-0485(2002)032⟨1522:SDMOTD⟩2.0.CO;2

Lele, R., Purkey, S. G., Nash, J. D., MacKinnon, J. A., Thurnherr, A. M., Whalen,

C. B., ... Talley, L. D. (2021, November). Abyssal Heat Budget in the Southwest Pacific Basin. *Journal of Physical Oceanography*, *51*(11), 3317–3333. Retrieved 2021-11-22, from https://journals.ametsoc.org/view/journals/phoc/51/11/JPO-D-21-0045.1.xml (Publisher: American Meteorological Society Section: Journal of Physical Oceanography) doi: 10.1175/JPO-D-21-0045.1

Lumpkin, R., & Speer, K. (2007). Global Ocean Meridional Overturning. *Journal of Physical Oceanography*, *37*(10), 2550–2562. Retrieved from http://dx.doi.org/10.1175/JPO3130.1 (ISBN: 0022-3670) doi: 10.1175/JPO3130.1

Marques, G. M., Loose, N., Yankovsky, E., Steinberg, J. M., Chang, C.-Y., Bhamidipati, N., ... Zanna, L. (2022, September). NeverWorld2: an idealized model hierarchy to investigate ocean mesoscale eddies across resolutions. *Geoscientific Model Development*, *15*(17), 6567–6579. Retrieved 2022-10-27, from https://gmd.copernicus.org/articles/15/6567/2022/ (Publisher: Copernicus GmbH) doi: 10.5194/gmd-15-6567-2022

Marsh, R., Nurser, A. J. G., Megann, A. P., & New, A. L. (2000, May). Water Mass Transformation in the Southern Ocean of a Global Isopycnal Coordinate GCM. *Journal of Physical Oceanography*, *30*(5), 1013–1045. Retrieved 2024-01-09, from https://journals.ametsoc.org/view/journals/phoc/30/5/1520-0485_2000_030_1013_wmtits_2.0.co_2.xml (Publisher: American Meteorological Society Section: Journal of Physical Oceanography) doi: 10.1175/1520-0485(2000)030⟨1013:WMTITS⟩2.0.CO;2

Marshall, J., Jamous, D., & Nilsson, J. (1999). Reconciling thermodynamic and dynamic methods of computation of water-mass transformation rates. *Deep-Sea Research Part I: Oceanographic Research Papers*, *46*(4), 545–572. (ISBN: 0967-0637) doi: 10.1016/S0967-0637(98)00082-X

Maze, G., Forget, G., Buckley, M., Marshall, J., & Cerovecki, I. (2009, August). Using Transformation and Formation Maps to Study the Role of Air–Sea Heat Fluxes in North Atlantic Eighteen Degree Water Formation. *Journal of Physical Oceanography*, *39*(8), 1818–1835. Retrieved 2023-07-21, from https://journals.ametsoc.org/view/journals/phoc/39/8/2009jpo3985.1.xml (Publisher: American Meteorological Society Section: Journal of Physical Oceanography) doi: 10.1175/2009JPO3985.1

McDougall, T., Feistel, R., Millero, F., & Jackett, D. (2009). The international thermodynamic equation of seawater 2010 (teos-10): Calculation and use of thermodynamic properties.

McDougall, T. J., Groeskamp, S., & Griffies, S. M. (2014). On geometric aspects of interior ocean mixing. *Journal of Physical Oceanography*, *44*, 2164–2175.

Megann, A. (2018, January). Estimating the numerical diapycnal mixing in an eddy-permitting ocean model. *Ocean Modelling*, *121*, 19–33. Retrieved 2022-12-19, from https://www.sciencedirect.com/science/article/pii/S1463500317301762 doi: 10.1016/j.ocemod.2017.11.001

Molenkamp, C. R. (1968, April). Accuracy of Finite-Difference Methods Applied to the Advection Equation. *Journal of Applied Meteorology and Climatology*, *7*(2), 160–167. Retrieved 2023-08-25, from https://journals.ametsoc.org/view/journals/apme/7/2/1520-0450_1968_007_0160_aofdma_2_0_co_2.xml (Publisher: American Meteorological Society Section: Journal of Applied Meteorology and Climatology) doi: 10.1175/1520-0450(1968)007⟨0160:AOFDMA⟩2.0.CO;2

Nurser, A. G., & Griffies, S. M. (2019). Relating diffusive surface salinity fluxes to boundary freshwater and salt fluxes. *Journal of Physical Oceanography*, *49*, 2365-2376. doi: 10.1175/JPO-D-19-0037.1

Nurser, A. J. G., Marsh, R., & Williams, R. G. (1999, July). Diagnosing Water Mass Formation from Air–Sea Fluxes and Surface Mixing. *Journal of Physical Oceanography*, *29*(7), 1468–1487. Retrieved 2023-10-

18, from https://journals.ametsoc.org/view/journals/phoc/29/7/1520-0485_1999_029_1468_dwmffa_2.0.co_2.xml (Publisher: American Meteorological Society Section: Journal of Physical Oceanography) doi: 10.1175/1520-0485(1999)029⟨1468:DWMFFA⟩2.0.CO;2

Purkey, S. G., & Johnson, G. C. (2012, September). Global Contraction of Antarctic Bottom Water between the 1980s and 2000s. *Journal of Climate*, *25*(17), 5830–5844. Retrieved 2022-11-28, from https://journals.ametsoc.org/view/journals/clim/25/17/jcli-d-11-00612.1.xml (Publisher: American Meteorological Society Section: Journal of Climate) doi: 10.1175/JCLI-D-11-00612.1

Ringler, T., Petersen, M., Higdon, R. L., Jacobsen, D., Jones, P. W., & Maltrud, M. (2013, September). A multi-resolution approach to global ocean modeling. *Ocean Modelling*, *69*, 211–232. Retrieved 2023-12-06, from https://www.sciencedirect.com/science/article/pii/S1463500313000760 doi: 10.1016/j.ocemod.2013.04.010

Saenz, J. A., Tailleux, R., Butler, E. D., Hughes, G. O., & Oliver, K. I. C. (2015, May). Estimating Lorenz's Reference State in an Ocean with a Nonlinear Equation of State for Seawater. *Journal of Physical Oceanography*, *45*(5), 1242–1257. Retrieved 2023-11-29, from https://journals.ametsoc.org/view/journals/phoc/45/5/jpo-d-14-0105.1.xml (Publisher: American Meteorological Society Section: Journal of Physical Oceanography) doi: 10.1175/JPO-D-14-0105.1

Sohail, T., Holmes, R. M., & Zika, J. D. (2023, April). Water-Mass Coordinates Isolate the Historical Ocean Warming Signal. *Journal of Climate*, *36*(9), 3063–3081. Retrieved 2023-08-01, from https://journals.ametsoc.org/view/journals/clim/36/9/JCLI-D-22-0363.1.xml (Publisher: American Meteorological Society Section: Journal of Climate) doi: 10.1175/JCLI-D-22-0363.1

Stanley, G. J., McDougall, T. J., & Barker, P. M. (2021). Algorithmic Improvements to Finding Approximately Neutral Surfaces. *Journal of Advances in Modeling Earth Systems*, *13*(5), e2020MS002436. Retrieved 2023-11-30, from https://onlinelibrary.wiley.com/doi/abs/10.1029/2020MS002436 (_eprint: https://onlinelibrary.wiley.com/doi/pdf/10.1029/2020MS002436) doi: 10.1029/2020MS002436

Stewart, K. D., Saenz, J. A., Hogg, A. M., Hughes, G. O., & Griffiths, R. W. (2014, April). Effect of topographic barriers on the rates of available potential energy conversion of the oceans. *Ocean Modelling*, *76*, 31–42. Retrieved 2022-12-19, from https://www.sciencedirect.com/science/article/pii/S1463500314000146 doi: 10.1016/j.ocemod.2014.02.001

Sverdrup, H., Johnson, M., & Fleming, R. (1942). The Oceans: Their Physics, Chemistry and General Biology. *Oceanography*, 1104. (arXiv: 1011.1669v3 ISBN: 9788578110796) doi: 10.2307/210609

Tamsitt, V., Abernathey, R. P., Mazloff, M. R., Wang, J., & Talley, L. D. (2018, March). Transformation of Deep Water Masses Along Lagrangian Upwelling Pathways in the Southern Ocean: SOUTHERN OCEAN UPWELLING TRANSFORMATION. *Journal of Geophysical Research: Oceans*, *123*(3), 1994–2017. Retrieved 2019-01-02, from http://doi.wiley.com/10.1002/2017JC013409 doi: 10.1002/2017JC013409

Tesdal, J.-E., MacGilchrist, G. A., Beadling, R. L., Griffies, S. M., Krasting, J. P., & Durack, P. J. (2023). Revisiting Interior Water Mass Responses to Surface Forcing Changes and the Subsequent Effects on Overturning in the Southern Ocean. *Journal of Geophysical Research: Oceans*, *128*(3), e2022JC019105. Retrieved 2023-08-10, from https://onlinelibrary.wiley.com/doi/abs/10.1029/2022JC019105 (_eprint: https://onlinelibrary.wiley.com/doi/pdf/10.1029/2022JC019105) doi: 10.1029/2022JC019105

Toggweiler, J. R., & Samuels, B. (1998). On the Ocean's Large-Scale Circulation near the Limit of No Vertical Mixing. *Journal of Physical Oceanography*, *28*(9), 1832–1852. Retrieved from http://dx.doi.org/10.1175/1520-0485(1998)028%3C1832:OTOSLS%3E2.0.CO%5Cn2 (ISBN: 0022-3670) doi: 10.1175/1520-0485(1998)028⟨1832:OTOSLS⟩2.0.CO;2

Tziperman, E. (1986, April). On the Role of Interior Mixing and Air-Sea Fluxes in Determining the Stratification and Circulation of the Oceans. *Journal of Physical Oceanography*, *16*(4), 680–693. Retrieved 2021-05-27, from https://journals.ametsoc.org/view/journals/phoc/16/4/1520-0485_1986_016_0680_otroim_2_0_co_2.xml (Publisher: American Meteorological Society Section: Journal of Physical Oceanography) doi: 10.1175/1520-0485(1986)016⟨0680:OTROIM⟩2.0.CO;2

Urakawa, L. S., & Hasumi, H. (2012, August). Eddy-Resolving Model Estimate of the Cabbeling Effect on the Water Mass Transformation in the Southern Ocean. *Journal of Physical Oceanography*, *42*(8), 1288–1302. Retrieved 2023-08-25, from https://journals.ametsoc.org/view/journals/phoc/42/8/jpo-d-11-0173.1.xml (Publisher: American Meteorological Society Section: Journal of Physical Oceanography) doi: 10.1175/JPO-D-11-0173.1

Urakawa, L. S., & Hasumi, H. (2014, February). Effect of numerical diffusion on the water mass transformation in eddy-resolving models. *Ocean Modelling*, *74*, 22–35. Retrieved 2023-08-25, from https://www.sciencedirect.com/science/article/pii/S1463500313002047 doi: 10.1016/j.ocemod.2013.11.003

Walin, G. (1982, January). On the relation between sea-surface heat flow and thermal circulation in the ocean. *Tellus*, *34*(2), 187–195. Retrieved 2020-02-10, from https://doi.org/10.3402/tellusa.v34i2.10801 doi: 10.3402/tellusa.v34i2.10801

Winters, K. B., Lombard, P. N., Riley, J. J., & D'Asaro, E. A. (1995, April). Available potential energy and mixing in density-stratified fluids. *Journal of Fluid Mechanics*, *289*, 115–128. Retrieved 2021-06-09, from https://www.cambridge.org/core/journals/journal-of-fluid-mechanics/article/available-potential-energy-and-mixing-in-densitystratified-fluids/A45F1A40521FF0A0DC82BC705AD398DA (Publisher: Cambridge University Press) doi: 10.1017/S002211209500125X

Zika, J. D., England, M. H., & Sijp, W. P. (2012, May). The Ocean Circulation in Thermohaline Coordinates. *Journal of Physical Oceanography*, *42*(5), 708–724. Retrieved 2023-08-31, from https://journals.ametsoc.org/view/journals/phoc/42/5/jpo-d-11-0139.1.xml (Publisher: American Meteorological Society Section: Journal of Physical Oceanography) doi: 10.1175/JPO-D-11-0139.1

Zika, J. D., & Taimoor, S. (2023, July). An optimal transformation method for inferring ocean tracer sources and sinks. *EGUsphere*, 1–25. Retrieved 2024-02-27, from https://egusphere.copernicus.org/preprints/2023/egusphere-2023-1220/ (Publisher: Copernicus GmbH) doi: 10.5194/egusphere-2023-1220